Origin and metallogenic significance of alkali metasomatism in the Paleoproterozoic Mapedi Formation, Kalahari Manganese Field, South Africa

A thesis submitted in fulfilment of the requirements for the degree of

Master of Science

At

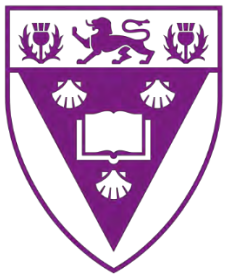

RHODES UNIVERSITY

Where leaders learn

By

Emmanuella Ikwen

Supervisor: Professor Steve Prevec (Rhodes University)

Co-Supervisor: Professor Harilaos Tsikos (University of Patras)

Declaration

I, **Emmanuella Ikwen**, student number **g16i1440**, hereby declare that this thesis, titled "**Origin and metallogenic significance of alkali metasomatism in the Paleoproterozoic Mapedi Formation, Kalahari Manganese Field, South Africa**" is my own work and information from other publications is adequately referenced. It is being submitted in fulfilment of the degree Master of Science in geology at the department of geology, faculty of science, Rhodes University.

Name of candidate: Emmanuella Ikwen Signature: 

Signed: on 17th of January 2023

Acknowledgements

I would like to thank my supervisor Prof. Steve Prevec for his support and encouragement while working on this thesis, and for making a very challenging experience substantially more bearable. I would also like to acknowledge and thank my former professor and supervisor, Prof. Harilaos "Hari" Tsikos for giving me the opportunity to work with him under the PRIMOR research group, and for providing me with a funding opportunity (through PRIMOR) to carry out this research. I also thank him for the advice, guidance, and friendship he has so freely given me throughout the course of my academic career. I thank Dr. Xolane Mhlanga for always being ready to help me and for being so generous with his time and insight, I deeply appreciate his help and support.

I would also like to thank my family for their consistent love and belief in me, and my mother specially, for always going out of her way to support and nurture my dreams. I would like to thank all my wonderful friends, including Gideon Onah, Chiamaka Onyekwuluje, and Dupe Ojo, for the great memories and experiences that were some of the best highlights of this entire process, I am deeply grateful for their love, support, and friendship. Finally, I'd like to acknowledge and thank Shalom Effiom, for being instrumental in encouraging me across the finish line, this thesis would not be finished without his support.

Abstract

The occurrence of alkali-rich metasomatic assemblages has been widely reported in various regions of the Kalahari Manganese Field (KMF). This alkali metasomatism has been characterized by the secondary introduction of elements such as K, Na, Li, Ba, P, V, Zn, As, amongst others. This study further explores the possibility of widespread alkali metasomatism in the KMF by reporting on and examining the occurrence of sugilite and other alkali-rich minerals at the contact between the Transvaal and Olifantshoek Supergroups in the Hotazel Mine area of the north-eastern KMF. The lithologies observed at the contact show macroscopic (such as cross cutting veins) and microscopic evidence of hydrothermal alteration.

Using analytical methods such as X-ray diffraction, X-ray fluorescence, and scanning electron microscopy, results showed that in the north-eastern region of the KMF, the metasomatism observed at the Transvaal-Olifantshoek contact is mainly characterized by enrichment in sodium, and the occurrence of sodium minerals, predominantly in the form of aegirine. The aegirine forms exclusively in the quartzites of the Mapedi Formation along with minerals such as sugilite, baryte, banalsite, amongst others. Albite also occurs within the quartzites, but also within the Mapedi red shales. The secondary nature of these minerals is established by geochemical comparisons with pristine, as well as alkali-metasomatized samples of the same formation which were obtained from other parts of the KMF and Postmasburg. These comparisons showed that the Mapedi quartzites in the north-eastern KMF have undergone extensive oxidation compared to samples of the same formation which were obtained from Postmasburg. The north-eastern quartzites have an average hematite abundance of 17 wt.% compared to Postmasburg quartzite which have an average of 7 wt.% hematite. Furthermore, some quartzite samples contained up to 40 wt.% in hematite content. The comparisons also showed that Mapedi quartzites from the north-eastern KMF are substantially more sodium enriched compared to Mapedi quartzites from the Postmasburg region, which on average have sodium oxide content below detection limits.

Geochemical comparisons were made between pristine Hotazel Formation samples from north-western KMF (Gloria Mine) and samples obtained from the north-eastern KMF (Hotazel Mine). Results showed that the samples obtained from the top of the Hotazel Formation (in the Hotazel

mine area) are likely altered hematite lutite and not Banded Iron Formation, evident by their substantially high manganese oxide content (over 30 wt.% in some cases). When compared to pristine samples, the lutite also showed evidence of hydrothermal alteration, predominantly in the form of phosphate and barium enrichment, evident by the occurrence of baryte and apatite. The alkali metasomatism occurring at the contact between the Transvaal and Olifantshoek Supergroups was shown to be predominantly characterized by enrichment in Na, K, Li, Al, Ba, Sr, and P. The metasomatism characterized in this study was also proposed to possibly post-date an earlier metasomatic event which was characterized by leaching of silica and extensive oxidation of the rocks observed at the Transvaal-Olifantshoek contact in the north-eastern KMF.

The occurrence of the alkali-rich minerals outlined above geochemically parallels other alkali-rich metasomatic assemblages reported in other parts of the KMF, as well as in the Postmasburg Manganese Field. Thus, based on the consistent occurrence of secondary, alkali-rich mineral assemblages across the KMF, characterized by the common occurrence of aegirine along with minerals such as sugilite and albite, there is evidence of a large-scale alkali metasomatism in the KMF.

This study also explores the possible role that the Transvaal-Olifantshoek unconformity might have played in acting as a major conduit for fluid propagation because the observed mineral assemblages occur right at the contact between the Hotazel and Mapedi Formations. The occurrence of the alkali-rich minerals predominantly around the unconformity, as well as the relative depletion of phosphates in stratigraphically deeper parts of the Hotazel suggest that the fluid metasomatism was aided by the Olifantshoek-Transvaal unconformity surface. This study concludes that there is evidence for a strong link between the metasomatism occurring at the contact between the Hotazel and Mapedi formations (in the north-eastern KMF) and what is observed in the broader KMF region.

Table of Contents

Table of Figures

List of Tables

1. INTRODUCTION

1.1 Background and rationale

The Kalahari Manganese Field (KMF) deposit of the Northern Cape, South Africa constitutes a major global resource of manganese ore (Beukes *et al*., 2016). This rich mineral reserve is estimated to possess approximately eight billion tons of manganese ore at grades ranging between 20–48% Mn (Tsikos *et al*., 2003). The KMF is hosted by the Hotazel Iron Formation of the Postmasburg Group, which forms part of the Transvaal Supergroup (Eriksson *et al*., 2006). The Transvaal Supergroup occurs in three separate basins; the Transvaal, Griqualand-West, and the Kanye basins (Eriksson *et al*., 2006). The Postmasburg group occurs in the Griqualand West basin, in the Northern Cape, South Africa (Eriksson *et al*., 2006). The Paleoproterozoic Transvaal Supergroup is estimated to be between 2.65–2.05 Ga (Beukes, 1983). Furthermore, the Ongeluk Formation beneath the Hotazel had been assigned an age of approximately 2.2 Ga (Cornell *et al*.,1998), but recent studies propose a new age of 2.43 Ga (Gumsley *et al*., 2017). In the context of the Hotazel Formation, the relationship between the ores and their host is described by Gutzmer & Beukes (1996) as three discrete, chemical, sedimentary ore bodies interbedded with banded iron formation (BIF). The KMF is mostly capped by calcrete and desert sand of the Kalahari Formation (Beukes *et al*., 2016), thus there are rarely any natural outcrops of the Hotazel Formation and its interbedded manganese ores. Only one of such an outcrop exists, and it is situated in the north-western part of the KMF called Blackrock. It was in this location where the manganese ores were first discovered and eventually mined (Beukes *et al*., 2016).

Manganese ores were first mined in the north of the KMF. The ore that that is found in the southern KMF differs in grade from those found in the northern KMF. In the north-western area and at a lesser scale, the north-eastern area, manganese ore of the higher-grade 'Wessels-type' is mined while in the southern KMF, the ore that is mined is termed lower-grade 'Mamatwan-type'. The reason for this distinction in grade is because the northernmost portion of the KMF has been extensively hydrothermally altered and therefore has been 'upgraded' relative to its southern counterpart (Gutzmer & Beukes, 1995).

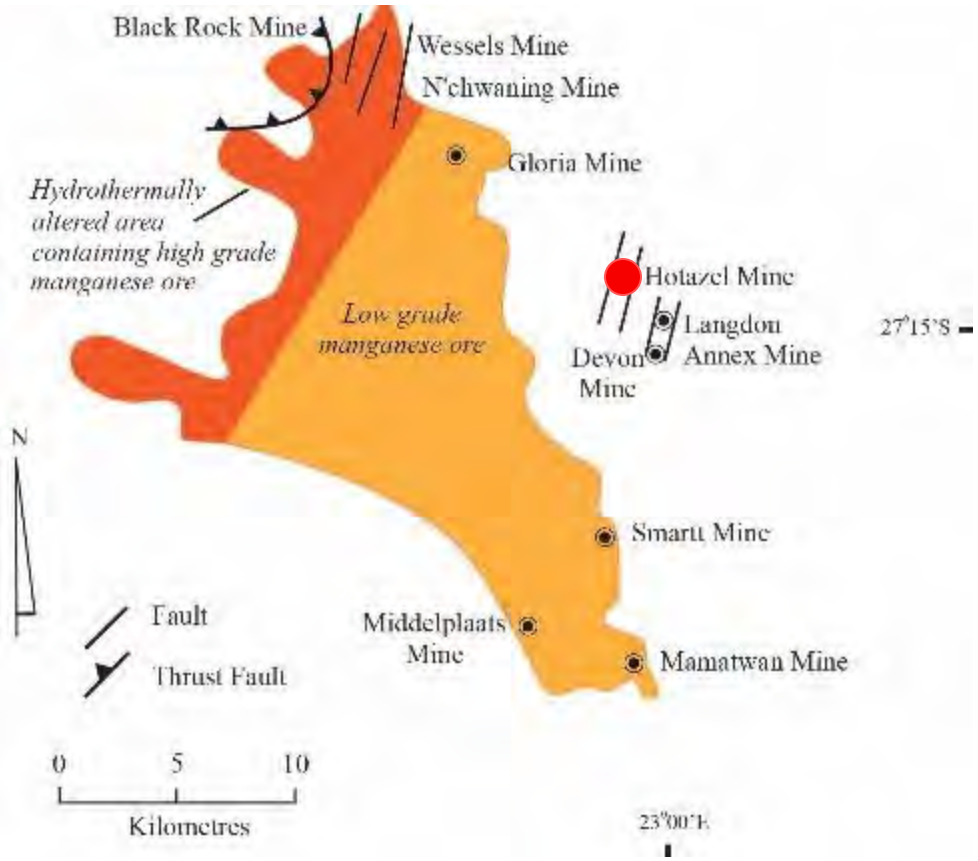

Figure 1. Locality map of the Kalahari manganese field, showing the major subdivision between low (Mamatwan type) and high (Wessels type) grade ore as well as important structural features (red dot indicates the locality of the Hotazel Mine where samples for this study were obtained) (After Mhlanga (2021)).

The result of this alteration which has been described as a fault-controlled, hydrothermal alteration (Gutzmer & Beukes, 1995) called the 'Wessels' event (at ~1.8 Ga) (Gutzmer & Beukes, 1996, 1997; Beukes *et al*., 2003) is that the Mamatwan-type ore remains a quartz-free, carbonate-rich, low-grade ore, capable of producing up to 38 wt.% in Mn metal content, while the Wessels-type ore was transformed into a carbonate-free, oxide-rich, high-grade ore, generally capable of producing > 44 wt.% in total Mn content (Tsikos & Moore, 2005). The low-grade ore is mainly in the form of kutnahorite and Mn calcite while the high-grade ore is rich in hausmannite, bixbyite and braunite (Tsikos & Moore, 2005).

The Wessels fluid event not only upgraded the ores in the north but through its expansive metasomatic effect, it produced an array of rare collectors' mineral specimens (Beukes *et al*., 2016). The mineral which first gained the KMF its popularity was rhodochrosite, but eventually a

host of other equally remarkable minerals were discovered amongst which was the purple mineral known as sugilite. Some other notable mentions include banalsite, kentrolite, kornite, sérandite, norrishite, and armbrusterite among many others (Costin *et al*., 2015). In all, Gutzmer & Beukes (1996a) identified at least 135 different species of minerals which occur in the northern KMF.

In the northern KMF, sugilite was first discovered in 1973 (Dunn *et al*., 1981) in the Wessels mine and then to a lesser extent in the N'chwaning mine (see figure 1 above). These mines are situated in the north-western area. In this area, the manganese ores and the adjacent wall-rocks have been metasomatized by highly oxidised alkali (sodium and potassium)-rich hydrothermal fluids to produce aegirine-rich rocks (Dixon, 1985, 1989; Tsikos & Moore, 2005). Along with sugilite, interesting silicate minerals including andradite, wollastonite, pectolite and vesuvianite also occur in the north-western KMF either as replacements or as zoned fracture and void fillings (Dixon, 1985; Gutzmer & Beukes, 1996).

After this discovery of sugilite in the north-western KMF, it was then reported in a study by Moore *et al*. (2011) that sugilite also occurs in borehole core from the Wolhaarkop breccia of the Bruce mine which is located south of the Sishen iron ore mine, approximately midway between Hotazel and Postmasburg (Cairncross, 2017). This was the first time that sugilite was found south of the KMF, in the Postmasburg Manganese Field (PMF) and this may have important implications with regards to the regional extent of the Wessels fluid event.

To elaborate further on the previous point, in the study by Moore *et al*. (2011), the occurrence of sugilite was in rocks of the basal Olifantshoek Supergroup in the Griqualand West basin (specifically in the eastern belt of the Maremane Dome). Immediately above the Wolhaarkop breccia is where massive hematite ores are regionally found (Moore *et al*., 2001; Cousins, 2016). Above the massive hematite mineralization, the base of the Mapedi Formation follows (Moore *et al*., 2001; Cousins, 2016). However, in the Maremane Dome area (i.e., the area which is also referred to as the PMF), it is referred to as the 'Gamagara Formation', and not the Mapedi Formation. In terms of lithology, the Gamagara and the Mapedi rocks, however, are the same (Moore *et al*., 2001; Cousins, 2016).

Thus, in the KMF, there is an occurrence of sugilite in close proximity to massive hematite ores, which are then stratigraphically overlain by red shales of the Mapedi Formation. Similarly, in the Maremane Dome, sugilite also occurs in close proximity to massive hematite ores which are

stratigraphically overlain by the red shales of the Gamagara Formation. In both cases, the massive hematite ores and the red shales are separated by a regional unconformity which extends from the KMF (Wessels) to Postmasburg and beyond (Moore *et al*., 2001; Cousins, 2016). This Gagamara/Mapedi unconformity (also referred to as the 'Transvaal-Olifantshoek unconformity' in this thesis), as well as the occurrence of similar patterns and contexts of mineralization, is the basis for the comparison between the sugilite mineralization occurring in the KMF and that which occurs in the PMF.

The sugilite that was discovered in the Wolhaarkop breccia occurs in association with serandite, albite, armbrusterite and norrishite, and Moore *et al*., (2011) proposed that the association of these minerals mineralogically and geochemically parallels what was previously observed in the north-western portion of the KMF as outlined above and that the discovery of such alkali-rich assemblages in the south, similar to those in the north provides evidence for the existence of widespread metasomatism by oxidised Na-K-rich hydrothermal fluids associated with the formation of iron and manganese ores adjacent to the Olifantshoek-Transvaal unconformity. Furthermore, discoveries of other exotic minerals in the PMF such as gamagarite by De Villiers (1943) and As-rich tokyoite and noélbensonite by Costin *et al*. (2015) further points out the geochemical similarities between the KMF and PMF and strengthens this possibility of widespread, regional-scale alkali metasomatism. To summarize, the alkali metasomatism that was considered to be concentrated in the north-western KMF seems to have been more extensive than previously believed and this may be deduced from the regional scale introduction of certain elements such as K, Na, Li, Ba, P, V, Zn, As, among others, not just into the rocks of the northern KMF but also into those of the PMF.

Like Moore *et al*. (2011), the focus of this study is at the stratigraphic contact between the rocks of the upper Transvaal Supergroup and the base of the Olifantshoek Supergroup. However, unlike the previous study, the samples being investigated here are sourced from the Hotazel mine area, in the north-eastern portion of the KMF, halfway between the northern- western Wessels mine in the Blackrock area and Mamatwan mine toward the south (see figure 1). The reason for, and the rationale behind this study is to compare the mineralization observed in the samples from Hotazel area with samples from the same formation found in the north-western KMF as well as similar samples from the PMF . The occurrence of these mineral assemblages found in the Hotazel area,

and their associated trace geochemical signatures may provide evidence for alkali metasomatism comparable to that which was observed and investigated in the north-western KMF by Gutzmer & Beukes (1995) and Tsikos & Moore (2005), and that which was observed and investigated in the southern KMF by Moore *et al*. (2011). Thus, there is a need to understand the origin and nature of this alkali metasomatism observed in the north-eastern KMF and its link (if indeed any such link exists) to the metasomatism that has been described in other regions of the KMF, as well as the PMF.

1.2 Geological setting

1.2.1 Regional geology

Deposited on the Kaapvaal craton, the Transvaal Supergroup is a platform succession spanning the end-Archaean/early Proterozoic period. It is made up of three unconformity-bounded sequences with outcrops of the supergroup located in the geographically separate Griqualand West, Transvaal and Kanye basins (Beukes, 1983). The eastern Transvaal basin circumscribes the Bushveld Igneous complex (Moore, Tsikos & Polteau, 2001), whereas the Griqualand West basin occurs in the western Kaapvaal margin (Smith & Beukes, 2016).

The Griqualand West basin, located in the Northern Cape province of South Africa, is sectioned into the lower Ghaap Group and the upper Postmasburg Group and exceeds 2000 m in total stratigraphic thickness (Tsikos *et al*., 2003). The Ghaap Group is mostly comprised of chemical sedimentary rocks. It begins with the Schmidtsdrif Subgroup, which contains fluvial, shallow marine and intertidal arenites as well as carbonates (Beukes, 1987). This is then followed by a thick succession of platform carbonates of the Campbellrand Subgroup. The Campbellrand Subgroup is divided into the Ghaap Plateau facies and the Prieska facies, and the two facies are divided by the Griquatown fault zone (Beukes, 1987). The Ghaap Plateau facies hosts the manganese ores of the PMF (Beukes, 1987).

The Campbellrand dolomites are overlain by the Kuruman Iron Formation, and Griquatown Iron Formation of the Asbestos Hills Subgroup. A regional, solution collapse unconformity separates the Campbellrand Subgroup and the Asbestos Hills Kuruman Iron Formation, and this

unconformity is host to massive hematite ores (Fairey *et al*., 2019). The iron ores have been described as being formed due to the process of slumping of the Asbestos Hills BIF into karstic sinkhole structures (Fairey *et al*., 2019). The deformed BIF is referred to as the Manganore Iron Formation. Dissolution of the Campbellrand dolomites which lie beneath the Asbestos Hills, led to residual buildup of insoluble chert, manganese, and iron, resulting in the formation of the Wolhaarkop breccia along the footwall of the collapsed Manganore Iron Formation (Fairey *et al*., 2019). The Ghaap Group terminates with the siliciclastic rocks and BIF of the Koegas Subgroup (Fairey *et al*., 2019).

Before the deposition of the successive Postmasburg Group, there was uplift and erosion of the Ghaap Group, therefore the Makganyene diamictites were deposited on an erosional unconformity which separates the Ghaap Group from the Postmasburg Group (Beukes, 1986). However, it is worth noting that this point has been disputed by Polteau *et al*. (2006) who reported field evidence of a conformable transition from the Koegas Subgroup to the overlying Makganyene Formation in some areas.

The Makganyene Formation is overlain by sub-aqueously extruded basaltic-andesitic pillow lavas and hyaloclastites of the Ongeluk Formation which extend 500-600 m in thickness (Gumsley *et al*., 2017). Conformably above the Ongeluk Formation are the rocks of the Voëlwater Subgroup which is sectioned into the lower Hotazel Iron Formation (which contains four iron formations interbedded with three sedimentary manganese layers) and the upper Mooidraai dolomites. The Mooidraai dolomites are preserved as erosional relicts in the KMF and regionally, the Voëlwater Subgroup is covered by 40 to 70 m calcrete of the Kalahari Formation (Grobbelaar *et al*., 1995).

The western portion of the Kaapvaal craton has been subject to two major tectonic events and as a result the Griqualand West basin is characterized by features of thrust faulting as well as folding which has led to strata duplication in certain regions of the basin (Grobbelaar *et al*., 1995).

A 270 km thrust fault associated with the Kheis orogeny runs from Black Rock in the north to Rooinekke in the south. It was named the Blackridge thrust by Van Wyk (1980). Beukes and Smit (1987) estimated that the horizontal displacement eastwards was from 35 to 125 km but the accuracy of this measurement is still the subject of debate (Grobbelaar *et al*., 1995). Thrusting at

Black Rock resulted in rocks of the Voelwater Subgroup being thrust onto the Olifantshoek sequence while at Rooinekke, thrusting resulted in the Ongeluk lavas of the Postmasburg Group being thrust over rocks of the Olifantshoek.

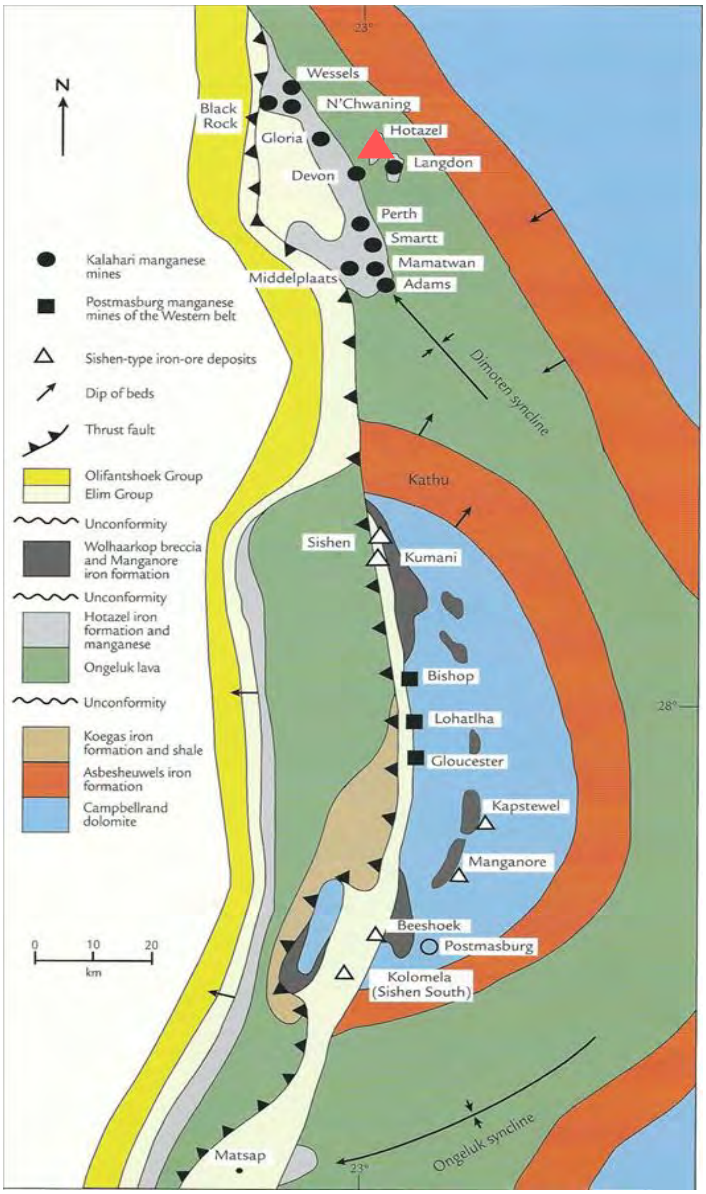

Figure 2. Map showing mine locations in the KMF, the Maremane Dome, Dimoten, and Ongeluk syncline (red triangle indicates the locality of the Hotazel Mine where samples for this study were obtained) (After Cape Minerals (2017)).

The thrusting is described as a single thrust which strikes roughly N-S and dipping 10˚ to the west. The extent and duration of the Kheis orogeny is still inconclusive. However, Beukes and Smit

(1987) assigned the thrusting event an age of 2-2.2 Ga, Stowe (1986) also assigned an age of 1.75-1.8 Ga.

The second tectonic event which occurred after the Kheis orogeny is the Kibaran orogeny. Characterized by complex, ductile deformation episodes, it had the effect of reactivating pre-existing faults in the Black Rock-Rooinekke area as well as developing new faults and lineaments, also with N-S trends (Grobbelaar *et al*., 1995). Due to stress relaxation after the extensive episode of ductile deformation, a tensional stress field developed resulting in the existing faults reverting to normal faults and thus leading to the formation of horsts and grabens (Grobbelaar *et al*., 1995). The Kibaran orogeny was assigned an age of ~1.2 Ga (Grobbelaar *et al*., 1995). The Wessels hydrothermal event has been linked to the Kibaran orogeny (Dixon, 1985; Beukes *et al*., 1995).

Gentle open folding occurring east of the Black Rock-Rooinekke thrust area resulted in the formation of the Dimoten syncline, the Maremane anticline (also known as the Maremane Dome) and the Ongeluk-Witwater syncline (Grobbelaar *et al*., 1995), as shown in figure 2. The folding led to uplift and erosion of the Transvaal strata. Dolomitic carbonate formations of the Campbellrand Subgroup of the Transvaal Supergroup were exposed at the unconformity surface in the core of the Dome, and BIFs of the Griquatown and Kuruman Formations were exposed at the northern and southern extremities and along the eastern flank of the Maremane Dome (Moore *et al*., 2011). Stratigraphic relationships along the western flank are more complex as a result of cover rocks of the Olifantshoek Supergroup and post-Olifantshoek thrusting and folding (Moore *et al*., 2011). This process of uplift and erosion of the Transvaal preceded the deposition of the Olifantshoek sequence (Van Wyk, 1980). Thus, between the Transvaal Supergroup and the Olifantshoek Supergroup lies an angular, erosional unconformity. In the central part of the eastern belt of the Maremane Dome, the red bed units which unconformably overlie the Campbellrand dolomites and Asbestos Hills IF is normally referred to as the Gamagara Formation, whereas the southern and northern extensions are known as the Mapedi Formation (Beukes & Smit, 1987).

The Gamagara/ Mapedi red beds, as well as quartzites, and iron rich conglomerates are found at the base of the Olifantshoek, these are then overlain by quartzites of the Lucknow Formation, which are overlain by green to red shales of the Paling member followed by the andesitic lava of the Hartley Formation (Land *et al*., 2017). The Olifantshoek is capped by the Volop subgroup, comprised of mostly quartzites and schists to a lesser extent. The mining that occurs in

Postmasburg, to the south of the KMF takes place along the Maremane Dome. It is along the Maremane Dome that mining of the Wolhaarkop breccia also takes place. This is because the tectonic processes discussed above have exhumed these rocks to the surface. In the northern KMF, major mining occurs along the structural axis of the Dimoten syncline, the strata are enriched along the Transvaal-Olifantshoek unconformity and hosts some of the richest manganese deposits in the world in the Hotazel, Mapedi and Lucknow Formations (Grobbelaar *et al*., 1995).

1.2.2 Local geology

The Hotazel Formation is the latest episode of iron formation deposition in the Transvaal Supergroup. It contains two major lithofacies; BIF and manganese ore, and these facies occur as cyclic units within the Hotazel (Tsikos & Moore, 1997). There are four distinct units of BIF interbedded with three manganese layers (see figure 3) and the BIF-Mn ore transitions are characterized by a red hematite-lutite facies (Tsikos & Moore, 1997). The Hotazel BIF showcases rhythmic bands of variable thickness which contain oxides (predominantly magnetite), silicates (greenalite, quartz, stipnomelane and minnesotaite) and carbonates (ankerite, siderite and calcite) (Tsikos *et al*., 2003). The Hotazel BIF at the base of the formation is the most oxide rich, in the central portions of the formation the BIF is more silicate rich whereas at the top of the formation, as the rocks grade into the overlying Mooidraai dolomites, the BIF is more carbonate rich (Tsikos & Moore, 1997). The composition of the hematite-lutite facies which mark the transition between BIF and Mn ore is made up of hematite and Mn carbonates, while the quartz free, oxide rich, laminated manganese layers predominantly contain braunite, manganese-bearing carbonates such as kutnahorite and manganoan calcite, and friedelite to a lesser extent (Tsikos *et al*., 2003). Formation of the high-grade Mn ores are thought to have been supported by fault-controlled, hydrothermal fluid flow, and lateral infiltration away from faults into the Hotazel Formation, accompanied by volume loss and compaction (Beukes *et al*., 1995; Gutzmer and Beukes,1995), as well as processes such as carbonate leaching and residual enrichment in Mn oxides (e.g., hausmannite, braunite) at the expense of carbonate rich protore (Tsikos *et al*., 2003).

Based on further evidence for these oxidation, leaching, and enrichment processes, especially in the uppermost portions of the Hotazel, as well as the observed spatial relationship between

enriched and dolomitized sections of the Hotazel Formation and the Hotazel-Olifantshoek unconformity, Tsikos *et al*. (2003) argued that these observations suggest that alteration and metal enrichment in the iron Formation could possibly have resulted from fluid flow focused along the overlying Hotazel-Mapedi unconformity surface and may not be largely fault controlled as proposed by Beukes *et al*. (1995).

The BIF units and the Mn ores show thickness relations that are opposite to one another (where one unit is thick, the other is thin (see figure 3)), and the Mn units, specifically the lower unit can reach up to 40-45 m in some areas (Tsikos & Moore, 1997). The age of the Hotazel Formation has been an issue of debate over the years, however recent radiometric U-Pb dating of the Ongeluk Formation has arguably placed the timing of the deposition of the overlying Hotazel Formation around the period of the Great Oxidation Event (between 2,46 and 2,43 Ga) (Gumsley *et al*., 2017).

The Mapedi Formation is proposed to have formed at ~1.93 Ga (Cornell *et al*., 1996). More recently, the age of ~ 2,426 ± 3 Ma has been assigned to the Ongeluk lavas (Gumsley *et al*., 2017), and a maximum age limit has been assigned to the Mapedi Formation that postdates the GOE by at least 100 Ma (Land *et a*l., 2017).

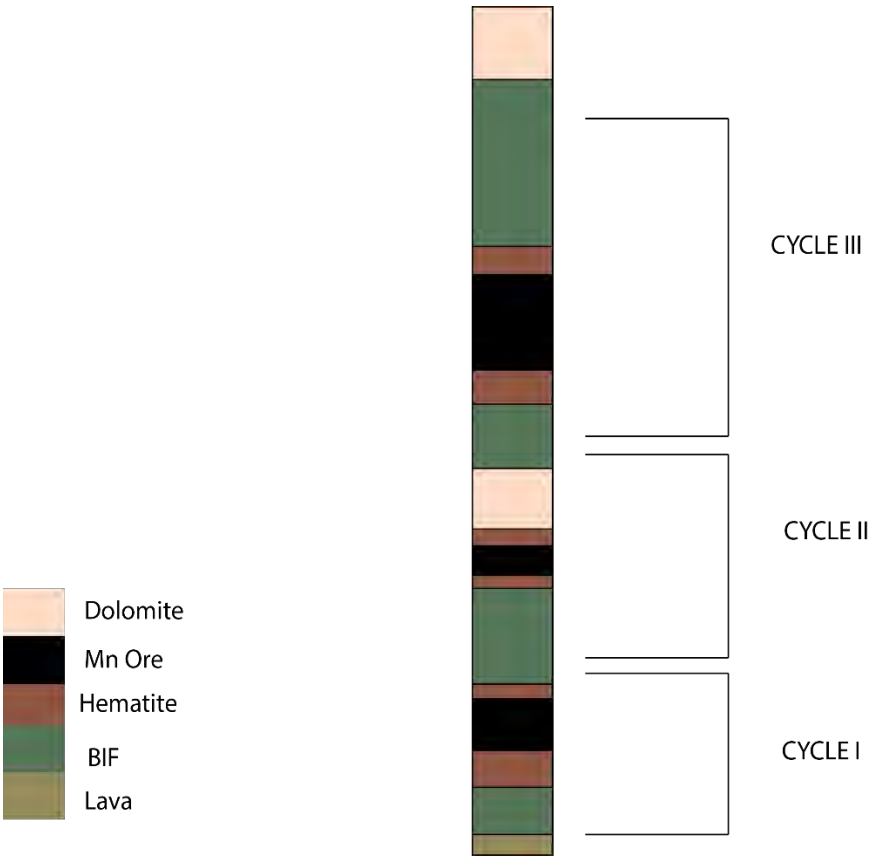

Figure 3. Simplified stratigraphy of the Hotazel Formation (After Tsikos & Moore (1997)).

The Mapedi Formation forms the basal unit of the Olifantshoek Supergroup and reaches 197 m in thickness (Beukes & Smit, 1987). It is dominated by discontinuous shale and quartzite, as well as conglomerate (predominantly in the basal member), and is separated from the Voëlwater Subgroup of the Transvaal by a regional angular unconformity. The region hosting the Mapedi Formation has experienced low-grade metamorphism, with maximum temperatures of 110 to 170°C and pressures <2 kbar (Miyano and Beukes, 1984). The red shales of the Mapedi Formation are characterized by a strongly hematite-enriched basal portion and are proposed to have formed by erosion, transport and deposition of hematite-rich lateritic sediment developed on top a provenance dominated by the Ongeluk volcanic rocks. This idea was however challenged by Land *et al*. (2017), where it was argued that the Mapedi strata show evidence of mineralogical and geochemical

signatures that oppose a basaltic andesite provenance and suggest a strong metasomatic overprint by highly alkaline, late diagenetic fluids.

1.3 Aims and objectives

The overarching aim of this study is to constrain the origin of the alkali-rich metasomatic mineral assemblages found in the basal quartzites of the Mapedi Formation and what implications that may have in the context of the metasomatic history of the broader KMF region. This will be done by employing mineralogical and geochemical techniques such as X-ray diffraction, X-ray fluorescence and scanning electron microscopy to characterize the mineralogy and geochemistry of the rocks of interest as well as to shed light on the possible metasomatic fingerprint of the hydrothermal fluid(s) responsible for their alteration. The study also aims to investigate what role the Transvaal-Olifantshoek unconformity could possibly have played in acting as a major conduit for the passage of the fluid(s) as well as the lithological controls which account for the formation of the observed mineral assemblages right at the unconformity of interest.

2. METHODOLOGY

2.1 Sample selection and analytical techniques

Representative samples were collected from exploration diamond drill core (supplied by Hotazel Mine) and consist of sixty-three half-core samples from boreholes DB87, DB88, DB89, W351 and UB189 (see figure 2 for sample locality). The samples span the immediate area surrounding the contact between the Transvaal-Olifantshoek unconformity and were retrieved from the Hotazel mine in the north-eastern KMF region. Drill core logging was carried out on these samples in order to determine the lithologies present as well as their stratigraphic relationships. Twenty-six representative samples were further selected based on homogeneity (i.e., they do not represent alteration fronts) and prepared for X-ray fluorescence analysis in order to determine the bulk geochemistry and the trace element abundances of the different lithologies observed. Twenty-five samples were also analyzed using X-ray diffraction to determine bulk mineralogy. Ten samples representative of the different lithological contacts were selected to be cut into thin sections and polished for petrography using a scanning electron microscope.

2.1.1 Petrography

Ten thin section samples representative of the lithological contact between the Hotazel and Mapedi Formations were studied under transmitted and reflected light using a Leica DM EP polarizing microscope from the Rhodes University geology department in order to observe possible mineral phases and any textural relationships of the mineral phases present.

2.1.2 X-ray diffraction analysis and SEM imaging

The 25 samples selected and prepared (crushed) for XRD were analysed at Rhodes University's chemistry department, on a Brucker X-ray diffractometer fitted with a Cu cathode. XRD spectra were obtained at 2θ angles between 10° and 99°. The data obtained was then analysed using the mineral identification software *Crystal Sleuth*, and in the case of each sample, its spectra was

compared with published spectra of the expected mineral phases in order to constrain its bulk mineralogy.

The 10 polished thin sections prepared for SEM analysis were first carbon-coated using the Q150T E High Vacuum Evaporator at the Rhodes University geology department. Point and ID (identification) analysis was then carried out on the thin section samples using the Rhodes University physics department's TESCAN Vega TS 5136LM SEM machine with an Oxford Instruments EDS, in order to qualitatively determine the mineral chemistry of the lithological contacts. The *INCA* software was used in visualizing mineral chemistry spectra obtained from the analysis as well as capturing back-scattered electron images.

2.1.3 Bulk geochemical analysis

Rare Earth Element (REE) abundances were measured using Inductively Coupled Plasma Mass Spectrometry (ICP-MS). Whole-rock major and trace element compositions were determined by XRF spectrometry on a PANalytical Axios Wavelength Dispersive spectrometer at the Central Analytical Facilities, Stellenbosch University, South Africa. Samples were crushed and major element analysis was carried out using fused glass disks and a 3kW Rh tube. The spectrometer was also fitted with analytical crystals, a gas-flow proportional counter and a scintillation detector. Bulk geochemistry data was produced for 26 samples from boreholes DB87, DB88, DB89, W351 and UB189. The matrix effects in the samples were corrected for by applying theoretical alpha factors and measured line overlap factors to the raw intensities measured with the SuperQ PANalytical software. The concentration of the control standards that were used in the calibration procedures for major element analysis fit the range of concentration of the samples.

3. RESULTS

3.1 Lithostratigraphy and macroscopic observations

3.1.1 Introduction

The focal point of this study is the contact between the Transvaal and Olifantshoek Supergroups, thus drill cores collected span just a few meters above and below the said contact. Observations of the material obtained from drill cores DB87, DB88, DB89, W351 and UB189 highlight three main, recurring lithological units.

1.) Ferruginous hematite-rich unit; This highly oxidized unit is characterized by a dark grey color with a strong reddish tint. It is massive in appearance and exhibits fine mm-scale laminations.

2.) Quartzite unit; this unit is made up of fine-grained quartzite with varying textures and colors. Sometimes very dull, smooth, massive, and showing no distinct coloration while in some places it is slightly coarser, tinted purple and has a sugary texture.

3.) Red shale unit; This unit is also very fine-grained and is characterized by a vibrant reddish color. It sometimes shows discontinuous laminations but it generally maintains a smooth massive, chalk-like texture.

3.1.2 Drill core DB87

A section of drill core DB87 spanning approximately 3.4 m was sampled. The material retrieved from this drill core intersection of the Hotazel-Mapedi contact indicates that a highly oxidized, hematite rich unit caps the Transvaal in the area. This lithological unit in drill core DB87 (figure 4) also shows features such as cross-cutting quartz veins and evidence of reworking of hematite within the unit. The hematite unit is grey in color and exhibits fine reddish laminations. Directly overlying it is the quartzite unit which marks the beginning of the Olifantshoek Supergroup. A feature observed in all the drill core intersections of the contact that were sampled, is the sharp contact between the hematite rich unit and the quartzite unit (figure 5).

Figure 4. Hematite-rich unit showing cross-cutting quartz veins (core DB87).

Figure 5. Hematite-quartzite contact (core DB87).

The quartzite unit sharply commences and shows different sub-facies within its lithology. The quartzite has a relatively coarser, sugary texture. It generally exhibits an off-white color but is also characterized by greenish, wavy microbands in other parts. The quartzite also shows evidence of replacement of grains by reddish hematite, while in other portions it displays a pink to purplish tint. Red shale directly overlies the quartzite unit, the shale is fine grained and massive in terms of texture. It is characterized by white colored, discontinuous laminations as well as cm-scale lenses of albite within the unit (see figure 6). The contact between the quartzite and shale unit is relatively more gradational.

Figure 6. Red shale with albite lenses (core DB87).

3.1.3 Drill core DB88

Approximately 2.2 m of drill core DB88 was logged and sampled. The lowermost unit sampled is the massive, fine-grained hematite unit which is also characterized by a grey color with a reddish tint. Along with fine laminations, it also shows secondary features such as mm-scale veins cutting across the lithology.

Figure 7. Hematite-quartzite contact (core DB88).

This unit terminates sharply and overlying it is the quartzite unit. The base of the quartzite unit, right above the contact with massive hematite is characterized by a strikingly purplish color (see figure 7), and this feature is consistent across most of the drill core intersections sampled for this study. The quartzite unit at the base is relatively finer grained and individual mineral grains cannot be observed in hand specimens.

Across the entire span of the quartzite unit, splotches of green can be observed, giving the quartzite a strong greenish tint in certain parts of the lithological unit. Further up in the quartzite unit, the

quartzite changes from a massive texture to a relatively coarser texture , with cm-sized hematite and smaller mm-sized aegirine crystals floating within a finer-grained quartz matrix (figure 8). Overlying the quartzite unit is the shale unit, it also has a massive texture and exhibits discontinuous lamination.

Figure 8. Hematite-bearing quartzite (core DB88).

Figure 9. Oxidized quartzite (core DB88).

3.1.4 Drill core DB89

Figure 10. Quartzite showing mottling effect (core DB89).

Approximately 4 m of drill core DB89 was logged and sampled in this study. The greyish-red, massive hematite unit at the base of the section also shows evidence of reworking, the reworked hematite crystals have an anhedral shape. Sharply overlying the hematite unit is the quartzite unit, which starts off with a fine-grained massive texture and is characterized by a purplish color.

Away from the contact, the quartzite unit transitions into a light color and shows a relatively coarser texture further up the unit due to the presence of cm-sized hematite and mm-sized aegirine. It also shows subtle mottling and, in some sections, it is characterized by straight and wavy laminations. Overlying the quartzite is the red shale unit. It is also fine-grained and massive in texture. It is characterized by a banded appearance due to larger, cm-thick , light colored bands as well as finer mm-sized discontinuous laminations (see figure 11).

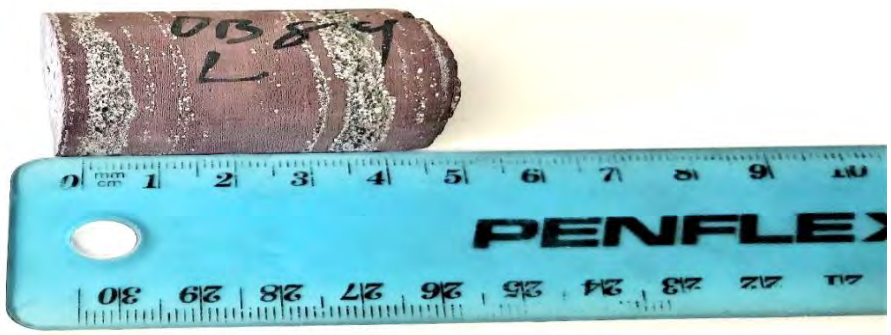

Figure 11. Laminated red shale (core DB89).

3.1.5 Drill core W351

Figure 12. Sugilite-bearing quartzite (core W351).

Approximately 5 m of drill core W351 (figure 12) was logged and sampled in this study. The base, mostly grey and massive hematite unit in this drill core is also thinly banded and shows light colored splotches across its thickness.

The transition between the hematite and quartzite units is sharp and immediate as observed in the other borehole cores.

Also observed at the contact is fine-grained, sugary textured, purplish colored quartzite. The color of the quartzite varies across the whole section, being light colored in some places and being varying shades of green and purple in others. Overlying the quartzite unit is the red shale unit.

3.1.6 Drill core UB189

Figure 13. Pink quartzite unit showing red-colored laminations (core UB189).

Approximately 1.4 m of drill core UB189 (figure 13) was logged and sampled in this study, the section starts off with massive hematite and there is also a sharp contact between the massive hematite and quartzite units. The quartzite unit is generally characterized by a chalky texture (similar to the red shale), and it has a red-colored, finely laminated appearance. The quartzite also has a purplish tint towards the hematite-quartzite contact, the purplish portion is characterized by a more fibrous texture. Away from the hematite-quartzite contact and towards the middle portion of the quartzite unit, there are mm-thick red laminations of hematite. Overlying the quartzite unit is the massive textured red shale unit.

Figure 14. Varying textures and colors within quartzite unit (core UB189).

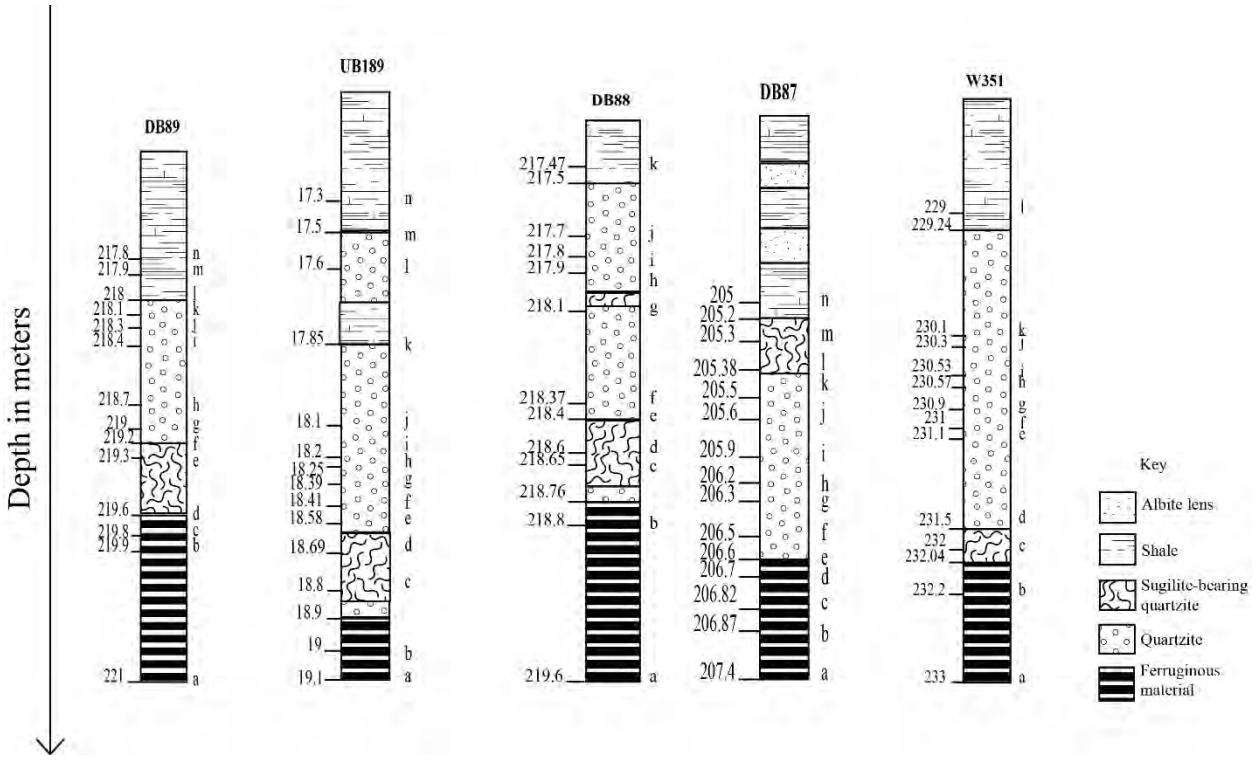

Figure 15. Stratigraphic logs of sampled suite.

Figure 15 shows the resultant stratigraphic logs based on the macroscopic observations outlined above. As previously stated, three lithological units have been identified and described. A basal hematite rich unit, followed by a sugilite-bearing quartzite unit, and at the top of the stratigraphy, a red shale unit occasionally containing albite lenses is observed. The Hotazel-Mapedi contact is represented by the contact between the ferruginous hematite-rich unit and the quartzite unit.

3.2 Mineralogy

3.2.1 Petrography

Petrography was carried out on thin section samples representative of the contact between the hematite-rich and quartzite units, in order to identify what major minerals characterize these sections of the stratigraphy. The thin section names correspond to the drill core samples they were prepared from (see figure 15). Quartz and hematite occur predominantly as expected, with hematite displaying its characteristic, red-colored internal reflection. Elongated crystals of aegirine also occur in association with albite.

a) Drill core DB87D

In thin section DB87D, albite and quartz, along with aegirine seem to dominate the matrix, with hematite occurring interstitially.

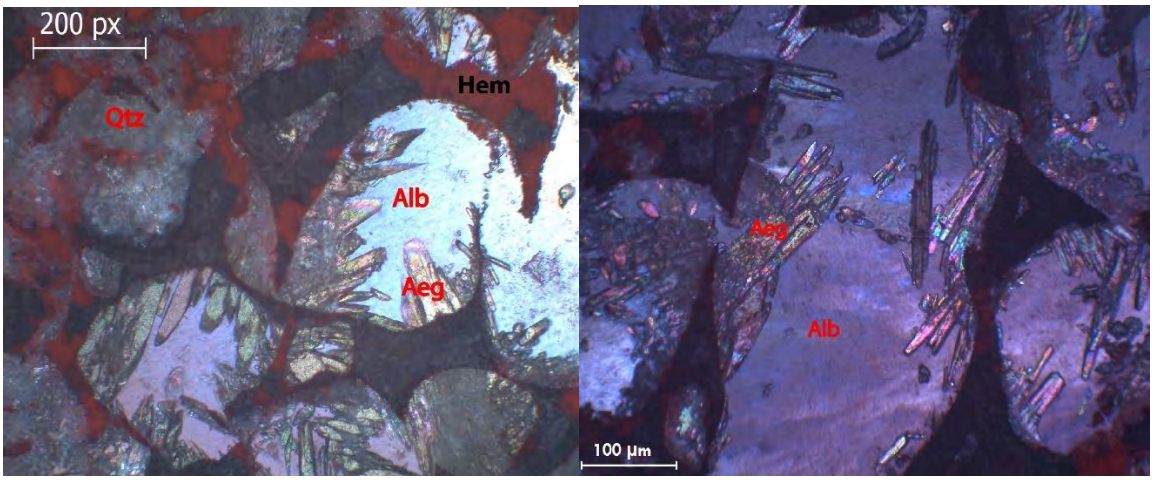

Figure 16. Thin section DB87D (contact between massive ferruginous hematite-rich unit and quartzite unit) under reflected light microscope showing textural relationship between quartz (Qtz), hematite (Hem), aegirine (Aeg), and albite(Alb).

b) Drill core DB88B

Thin section DB88B as shown figure 17 below depicts the sharp nature of the contact between the hematite-rich unit and the quartzite unit.

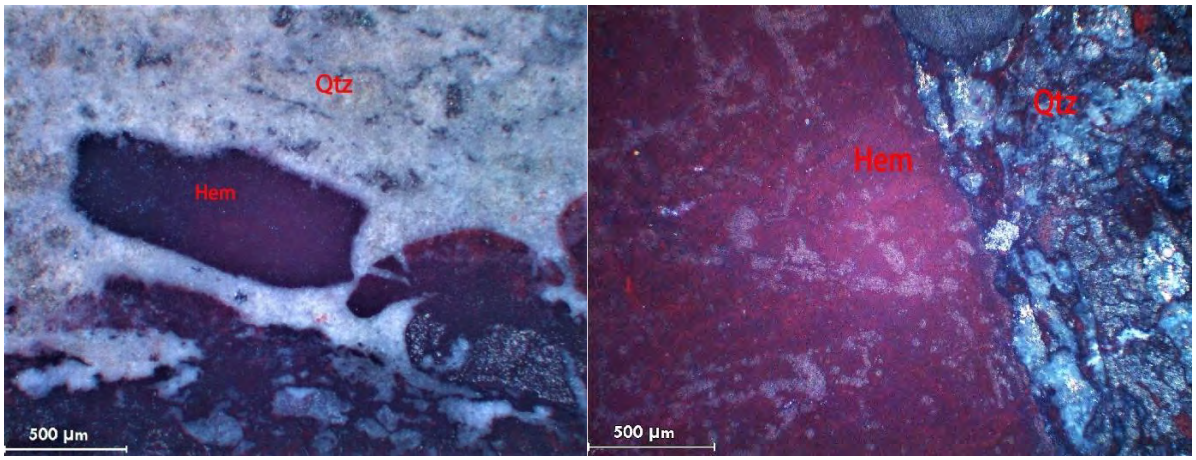

Figure 17. Thin section DB88B (contact between massive ferruginous hematite-rich unit and quartzite unit) under reflected light microscope showing textural relationship between quartz (Qtz), and hematite (Hem).

c) Drill core UB189B

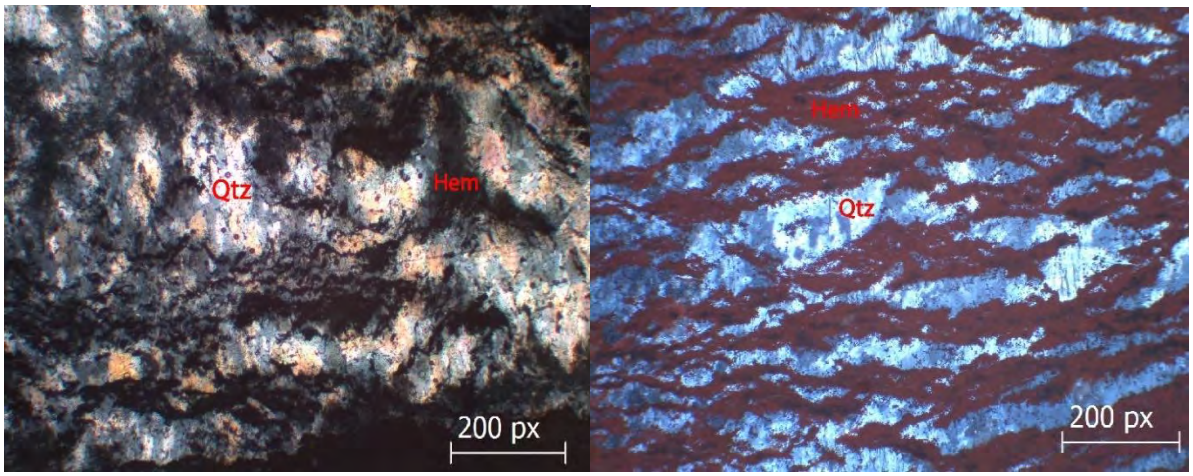

Figure 18. Thin section UB189B (contact between massive ferruginous hematite-rich unit and quartzite unit) under transmitted light (plane-polarized) (left) and reflected light (right)microscope showing textural relationship between quartz (Qtz), and hematite (Hem).

Thin section UB189B captures another textural relationship between quartz and hematite under a reflected light as well as transmitted light microscope. Hematite appears to occur as wavy laminations across the quartz matrix.

d) Drill core W351C

In thin section W351C quartz heavily dominates the contact with minor occurrences of hematite.

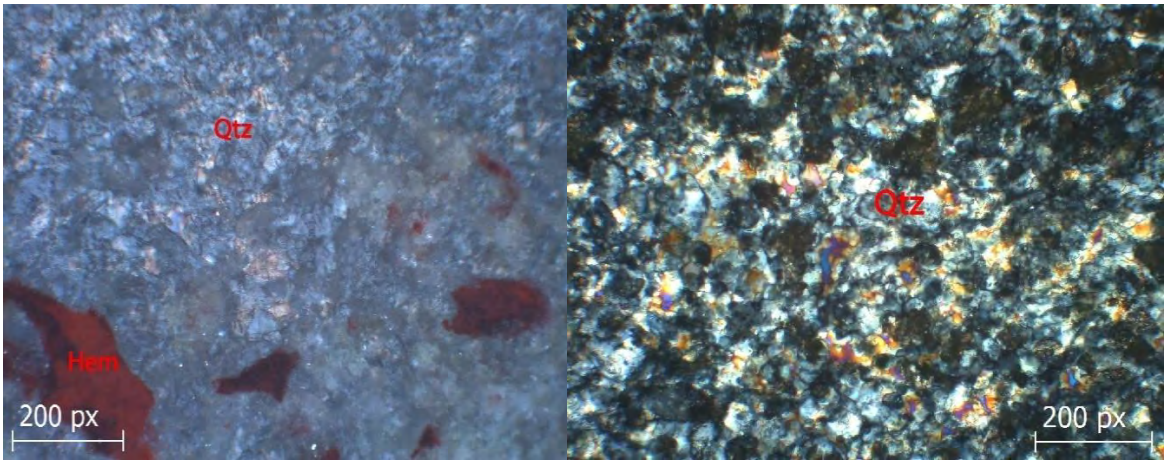

Figure 19. Thin section W351C (contact between massive ferruginous hematite unit and quartzite unit) under reflected light (left) and transmitted light (right) microscope showing textural relationship between quartz (Qtz), and hematite (Hem).

In summary, the minerals identified at the contact using petrography include; quartz, hematite, aegirine, as well as albite.

3.2.2 Scanning electron microscopy

Due to the very fine-grained nature of the rock samples, SEM analysis was carried out to compliment the petrography results discussed in section 3.2.1. The thin section samples representative of the lithological contacts were further observed using a scanning electron microscope.

Point and ID was carried out on thin sections DB87D and DB87E using scanning electron microscopy. The area analyzed is the contact between the ferruginous material and the quartzite section. Sugilite, hematite, and aegirine were identified in this thin section sample. Albite was also identified at the contact, mostly in association with aegirine, which is consistent with what results provided in the previous section.

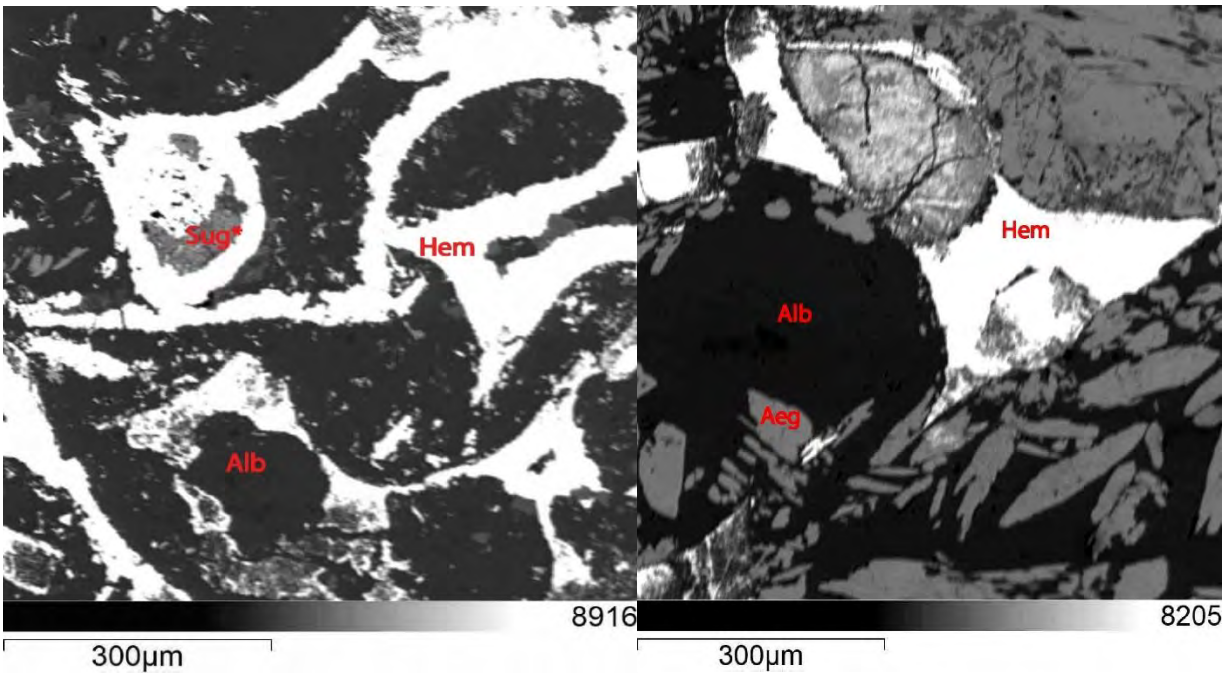

Figure 20. Drill core DB87D (hematite-quartzite contact), Sug= Sugilite, Hem= Hematite, Alb= Albite, *= inconclusive.

Petrography and SEM analysis indicate that the contact is characterized by interstitial occurrences of finer-grained hematite rich and sugilite , with aegirine and albite grains floating within the matrix. Aegirine appears to have a textural relationship with albite. It grows as prismatic crystals within albite crystals that are exhibiting a predominantly fairly rounded grain shape.

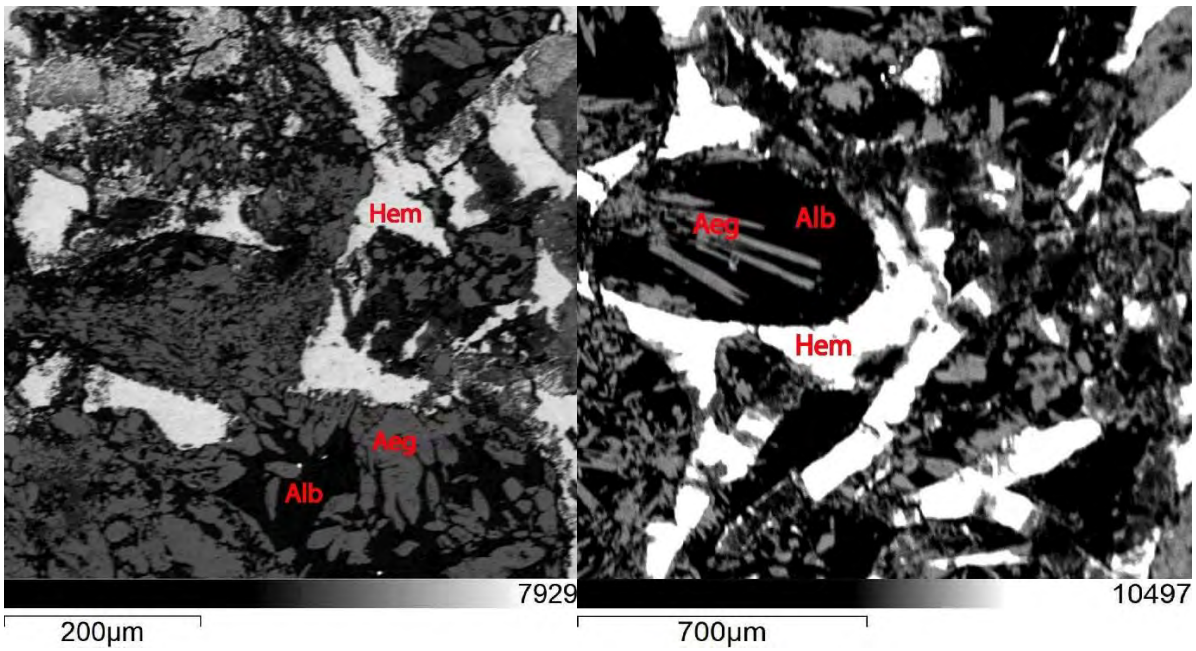

Figure 21. Drill core DB87E (hematite-quartzite contact), Hem= Hematite, Alb= Albite, Aeg= Aegirine.

Point and ID analysis was also carried out on thin sections DB88B1 and DB88B2, these sections are also representative of the contact between the ferruginous, hematite-rich material and the quartzite unit. These samples were further characterized by the presence of albite and aegirine, along with andradite, baryte, banalsite, and apatite sitting within a fine-grained hematite matrix.

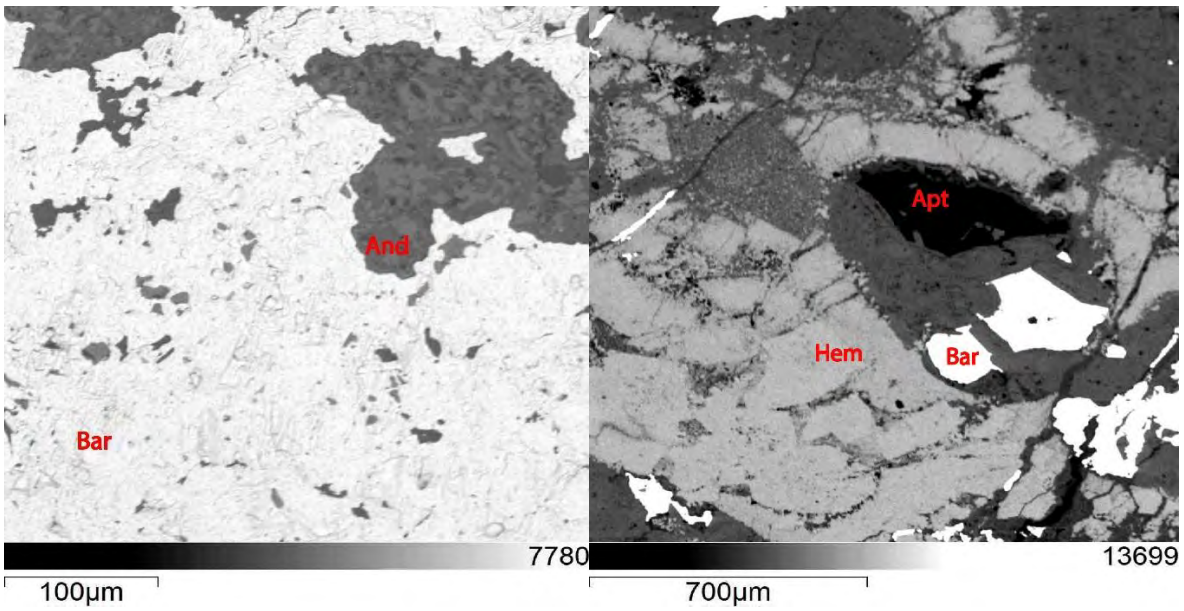

Figure 22 . Drill core DB88B1 (hematite-quartzite contact), Hem= Hematite, Apt= Apatite, Bar= Baryte.

Aegirine also shows up in this section as in textural association within albite, banalsite is associated with baryte.

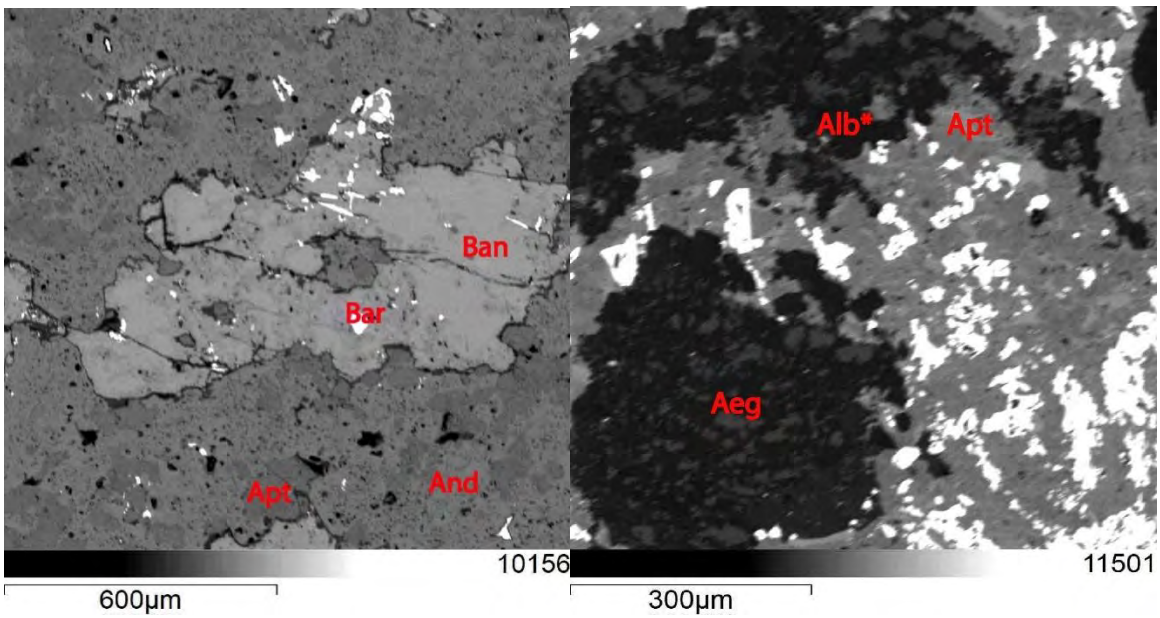

Figure 23. Drill core DB88B2 (hematite-quartzite contact), Apt= Apatite, Alb= Albite, Bar=Baryte, Ban=Banalsite, And=Andradite, Aeg= Aegirine, *=inconclusive.

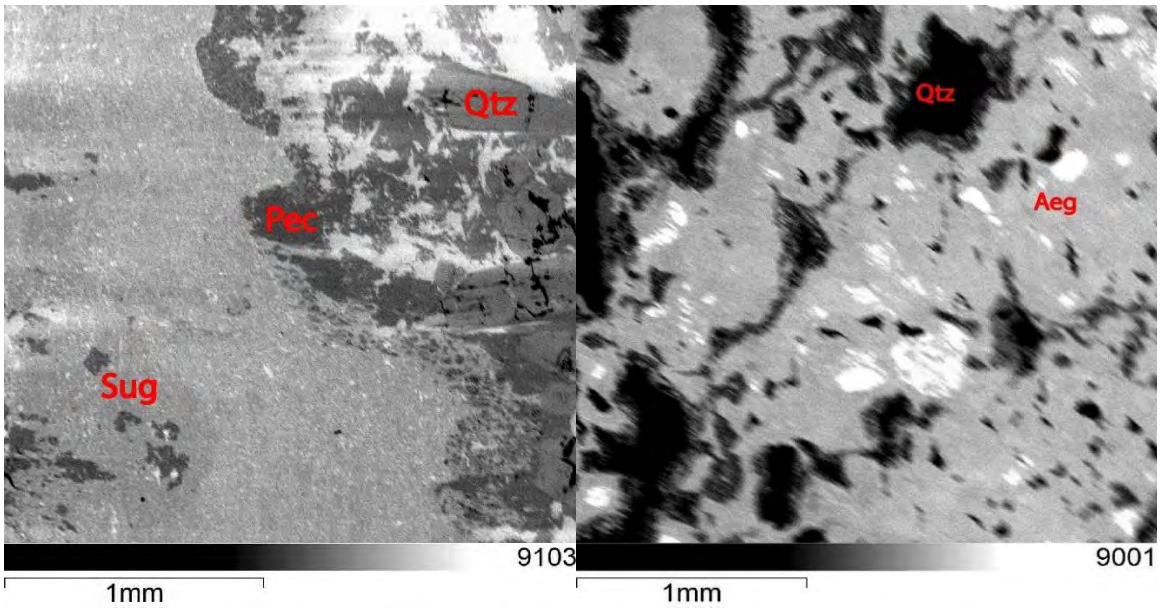

Figure 24**. **Drill core UB189C (left) and W351C (right) Qtz= Quartz, Aeg= Aegirine, Sug= Sugilite, Pec= Pectolite.

Drill core UB189C indicated the presence of pectolite in association with quartz and sugilite and drill core W351C confirmed the presence of aegirine along with quartz at the contact between the hematite-rich and quartzite units.

In summary, petrography and SEM analysis results suggest that the contact between the hematite and quartzite units, which is also representative of the contact between the Hotazel and Mapedi Formations, is characterized by the occurrence of a variety of minerals. These minerals include hematite, quartz, sugilite, albite, aegirine, baryte, banalsite, apatite, pectolite, and andradite. This mineral assemblage was identified consistently across the contact between the Hotazel and Mapedi Formations as preserved in all five drill core sections.

3.2.3 X-ray diffraction

XRD analysis was carried out in order to characterize the mineralogy of each discrete lithological unit identified within all five boreholes as shown in figure 15. As discussed in section 3.1, these units include; the ferruginous, hematite-rich unit, the quartzite unit , and the red shale unit.

a) Drill core DB87

X-ray diffraction results from drill core DB87 provided insight into bulk mineralogy. As expected, the hematite-rich unit consists of predominantly hematite. Some aegirine is detected in this section, attributable to the presence of thin layers of quartzite interlayering with the massive hematite. This is consistent with the general observation that aegirine tends to be associated with the quartzites sampled in this study.

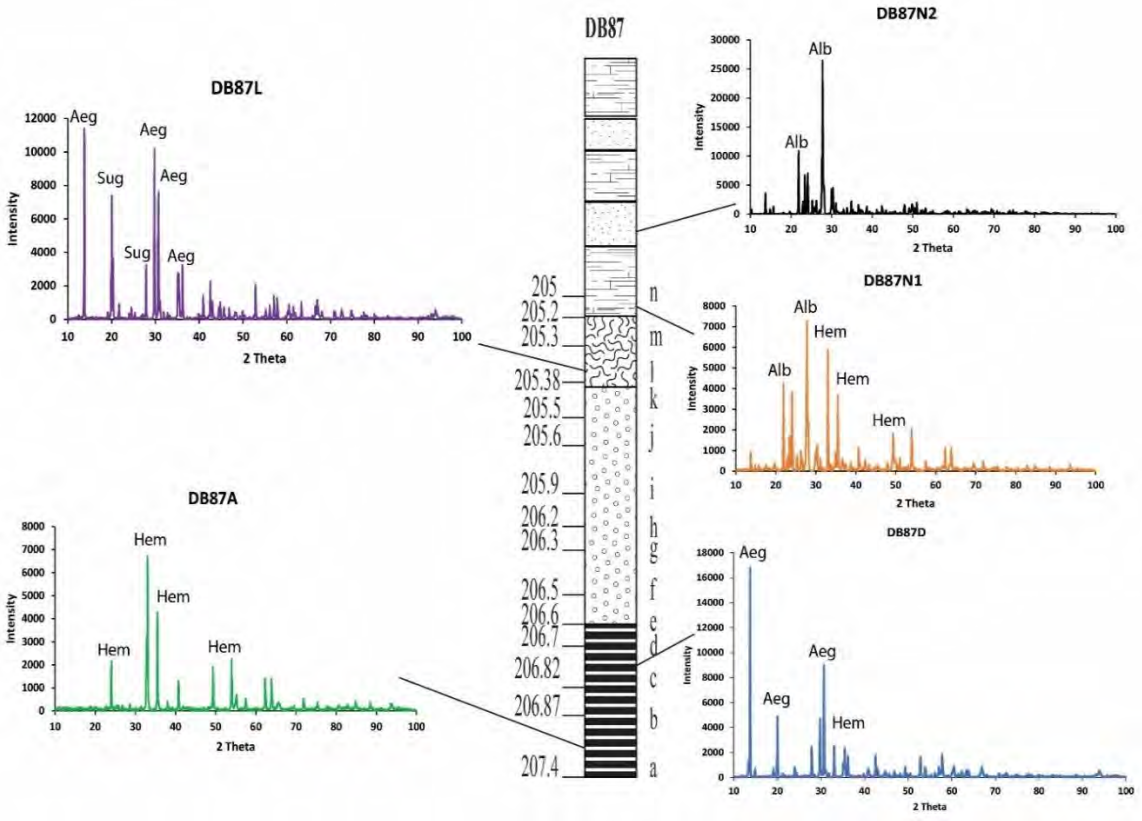

Figure 25. Drill core DB87 XRD data, Sug= Sugilite, Hem= Hematite, Alb= Albite, Aeg= Aegirine.

In this drill core section, toward the top of the quartzite layer, results confirmed the presence of sugilite as well as relatively higher concentrations of aegirine. In the red shale unit, hematite was

also identified along with albite. Figure 6 shows the red shale from this borehole exhibiting cm-scale, light colored lenses which consist of albite.

b) Drill core DB88

XRD analysis of drill core DB88 also confirmed that the bulk mineralogy of the hematite-rich unit consists of hematite. The quartzite unit consists mainly of quartz, aegirine, and sugilite. Hematite and baryte peaks were also present in this unit which is consistent with the oxidized nature of these quartzites. The red shale unit comprises of quartz, albite, and hematite.

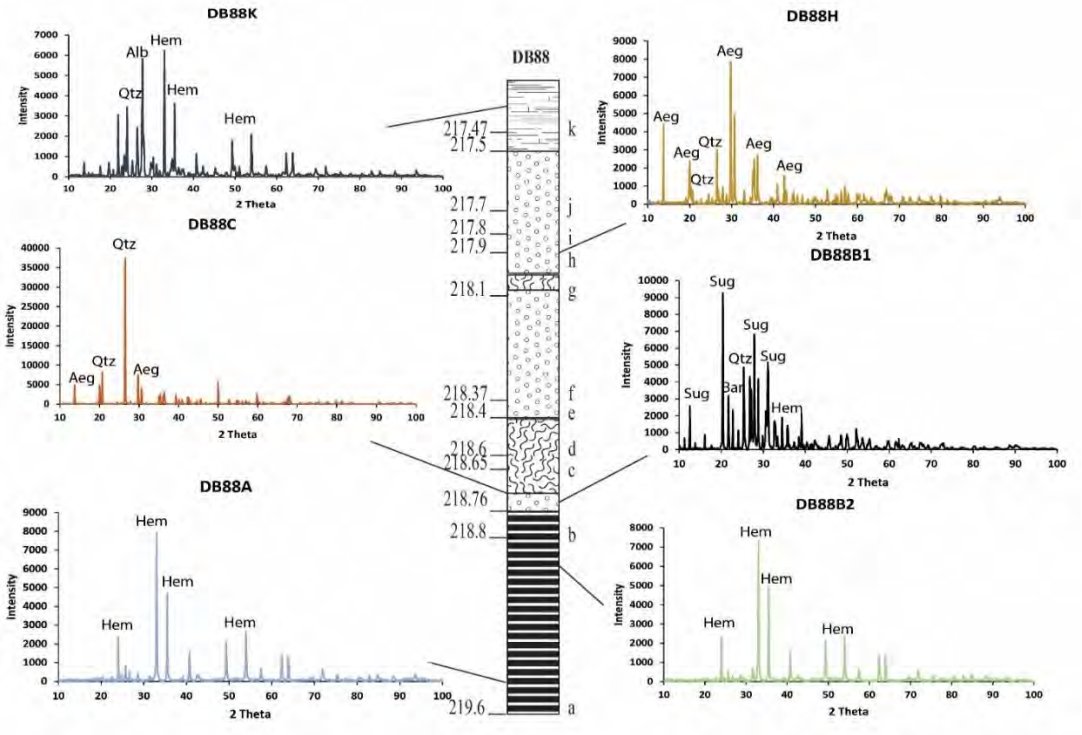

Figure 26. Drill core DB88 XRD data Sug= Sugilite, Hem= Hematite, Alb=Albite, Aeg= Aegirine, Qtz= Quartz, Bar= Baryte.

c) Drill core DB89

In hole DB89, the bulk mineralogy of the quartzite unit as well as the shale unit were also consistent with bulk mineralogy observed across the other drill core samples analyzed in this study. The quartzite unit returned peaks consistent with quartz, aegirine and sugilite, with sugilite showing relatively higher concentrations in this sample.

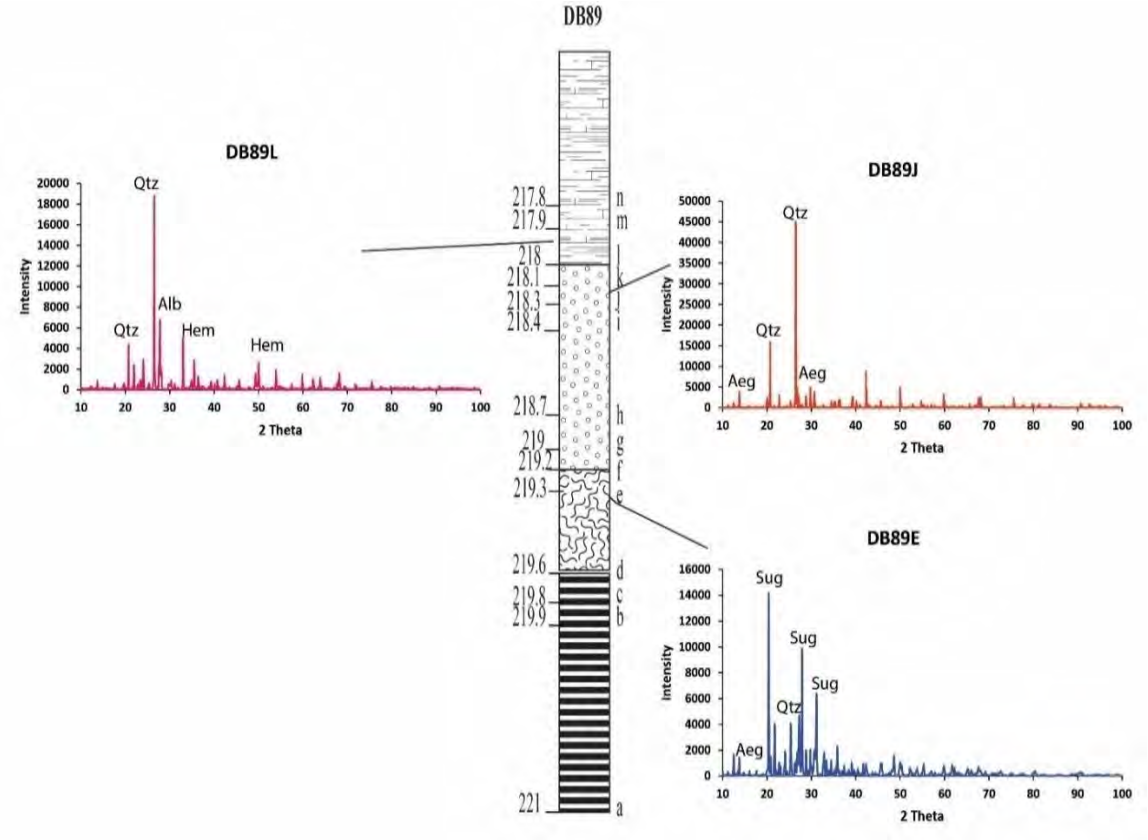

Figure 27. Drill core DB89 XRD data Sug= Sugilite, Hem= Hematite, Alb=Albite, Aeg= Aegirine, Qtz= Quartzite.

The red shale unit returned peaks consistent with quartz, albite, and hematite. A sample of the hematite-rich section of this drill core was not sent in for analysis due to a sampling error and thus no results were received for it for this section of the drill core.

d) Drill core UB189

XRD analysis of this sample also confirmed a hematite-rich unit at the base of the stratigraphy. There were also peaks in this section that are consistent with a manganese oxide mineral, possibly braunite, however this could be subject to reconsideration. The analyzed sample from the quartzite unit of this drill core returned peaks consistent with quartz, hematite and sugilite. The red shale unit returned peaks consistent with quartz and hematite.

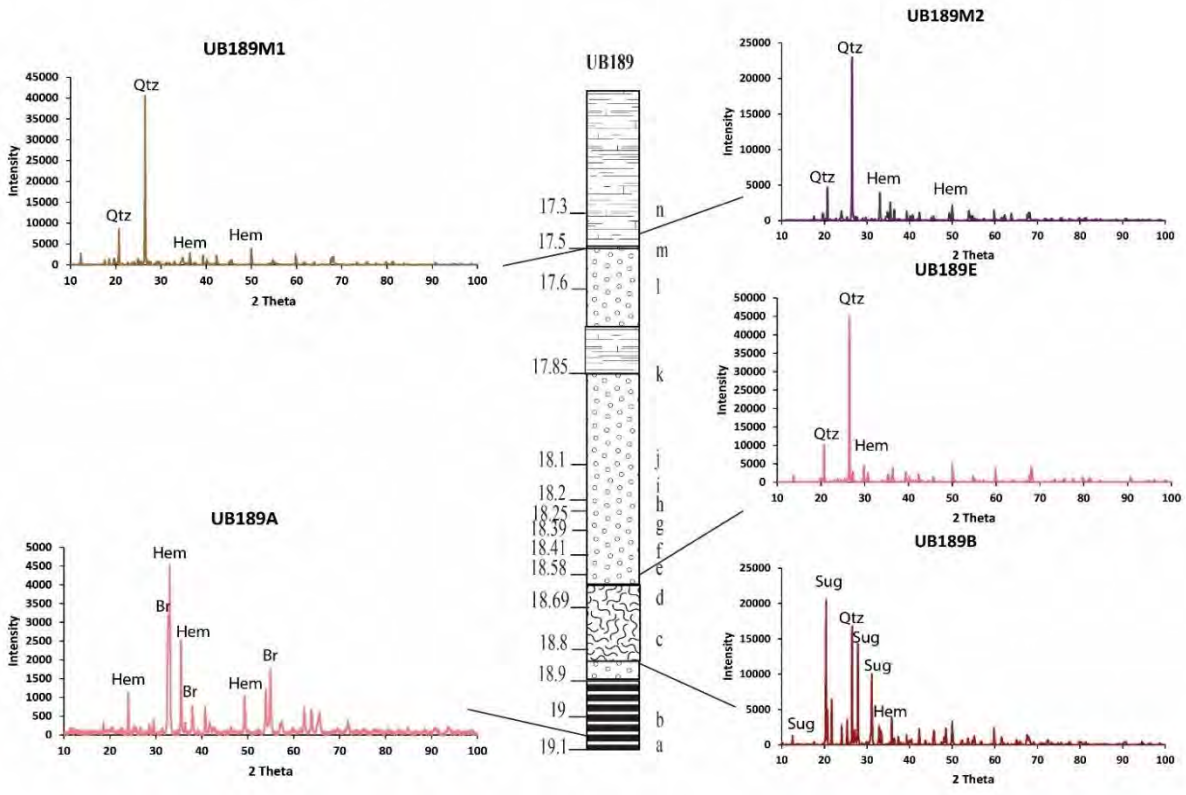

Figure 28. Drill core UB189 XRD data Sug= Sugilite, Hem= Hematite, Br= Braunite, Qtz= Quartzite.

e) Drill core W351

XRD analysis of drill core W351 returned consistent results as well in terms of bulk mineralogy for each lithology. The ferruginous section comprises of hematite, the quartzite section consists of quartz, sugilite and aegirine. The shale section consists of quartz predominantly with hematite content being relatively lower. This is consistent with its relatively less reddish color, and more silica rich grains.

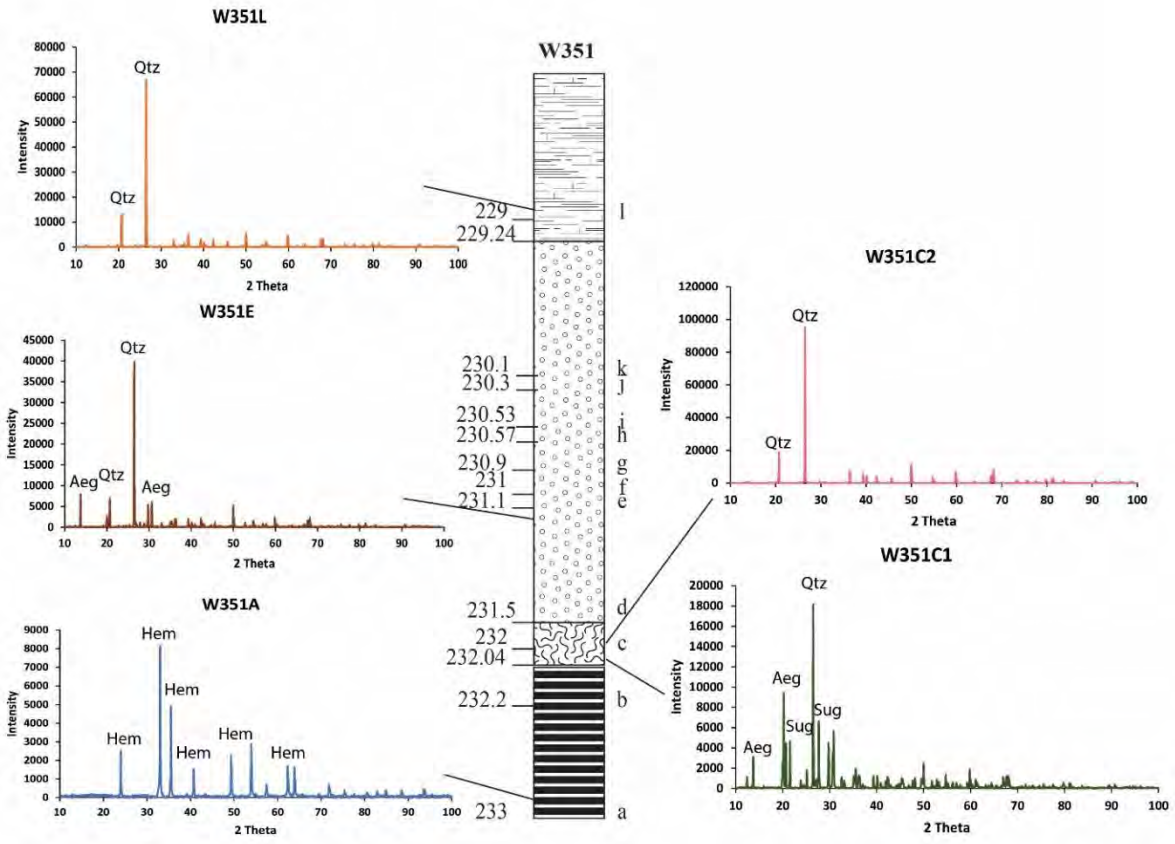

Figure 29. Drill core W351 XRD data Sug= Sugilite, Hem= Hematite, Aeg= Aegirine, Qtz= Quartzite.

In summary, XRD results showed that the mineralogy of the hematite-rich unit is characterized predominantly by hematite, the quartzite unit is characterized by quartz, sugilite, aegirines, hematite and baryte. The red shale unit is characterized by predominantly albite, quartz, and hematite.

3.3 Bulk Geochemistry

Bulk geochemical analysis was carried out on homogenous samples of the three lithological units in order to obtain the major oxide and trace element geochemistry of each unit (see appendix A for major, trace, and rare earth element abundances obtained from bulk geochemical analysis). For comparison of the samples with the standard shale element concentrations, the values of element concentrations within the samples were normalized against Post Archaean Australian Shale (PAAS) for each element respectively. For the purpose of representing the data in a concise manner when comparing bulk geochemical abundances, abundance values for all samples in each lithological unit have been averaged before being normalized against PAAS.

3.3.1 Hematite-rich unit

The bulk geochemistry results for the ferruginous samples are consistent with their mineralogy predominantly consisting of hematite, with iron oxide percentage values ranging from 48.04% - 94.55%. The wide range in iron contents will be elaborated on later. In three samples, manganese oxide content is curiously high (22.98% - 43.9%.) Thus, these samples are made up mostly of iron oxide and in some cases, manganese oxide is almost equally as abundant as iron oxide.

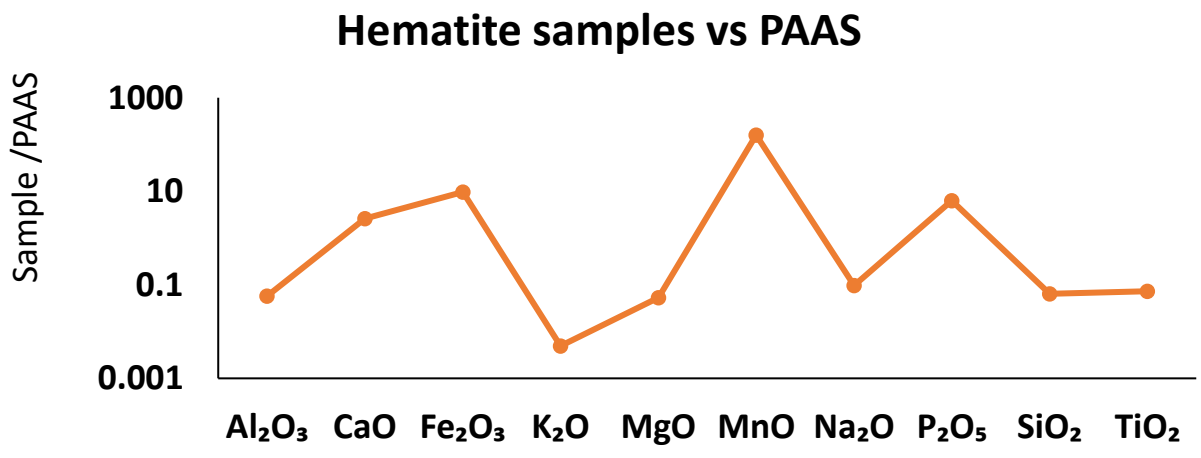

Figure 30. Average major oxide abundances of hematite samples relative to Post Archaean Australian Shale (n=6).

In terms of major oxide geochemistry, relative to PAAS the samples seem to be depleted in silica and alkali oxides. Along with an enrichment in iron and manganese oxide, there is also an enrichment in phosphate content (PAAS; Pourmand *et al*., 2012) .

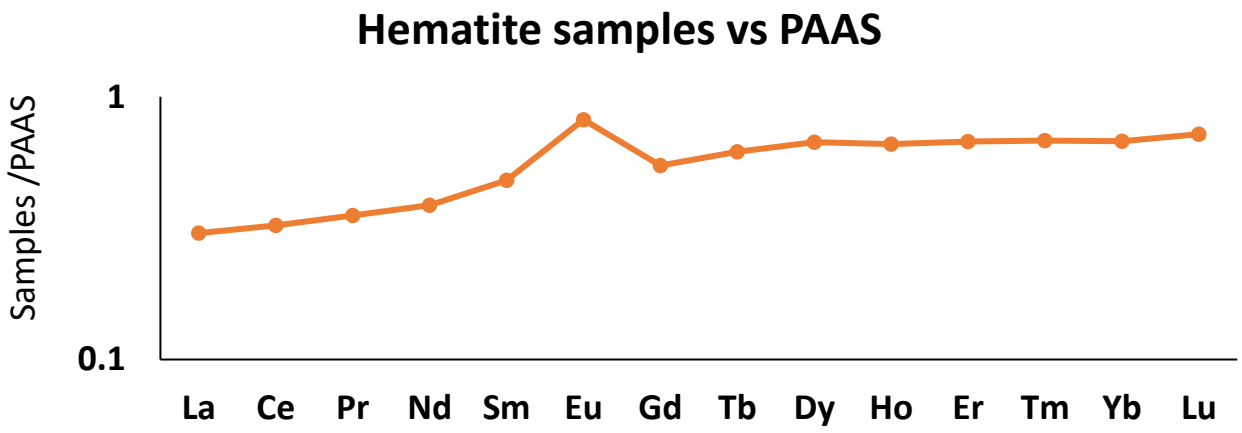

Figure 31. Average REE abundances of hematite samples relative to Post Archaean Australian Shale (n=6).

The hematite samples when plotted against PAAS REE abundances result in an REE plot with a positive slope. The plot shows that on average, the samples are less enriched in REEs compared to PAAS. The positive slope of the plot also indicates that on average, relative to PAAS, HREEs in these samples are more enriched than LREEs. These samples display a weak positive Eu anomaly.

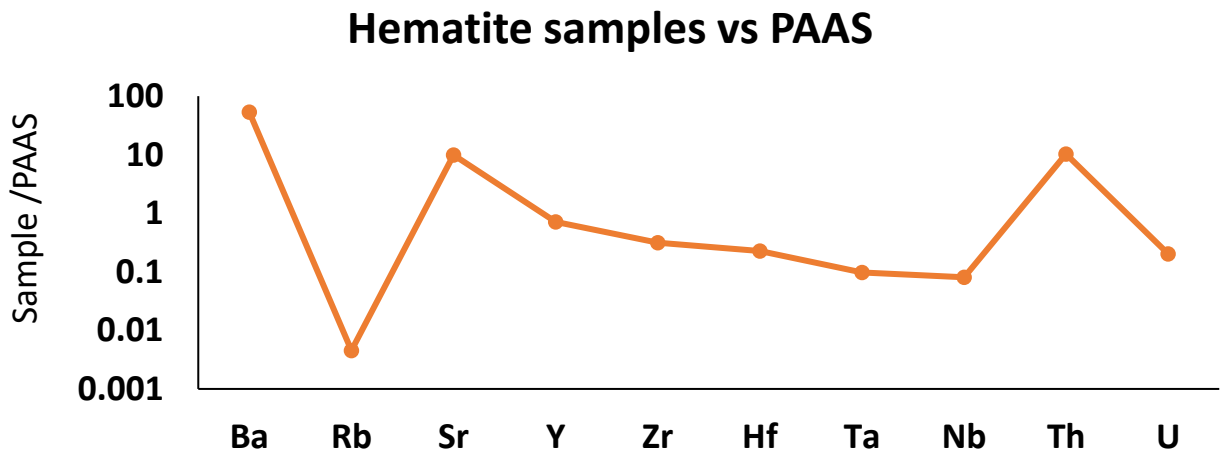

Figure 32. Average HFSE abundances of hematite samples relative to Post Archaean Australian Shale (n=6).

In terms of high field strength elements(HFSEs), the hematite samples are generally only slightly depleted relative to PAAS, except with regards to barium and strontium and thorium which are enriched in these samples. Rubidium depletion is possibly related to the low potassium content since rubidium is known to substitute for potassium in its crystal structures. These results are consistent with SEM results which qualitatively identify the presence of baryte, banalsite, and possibly its strontium counterpart stronalsite at the contact between the ferruginous material and the quartzites.

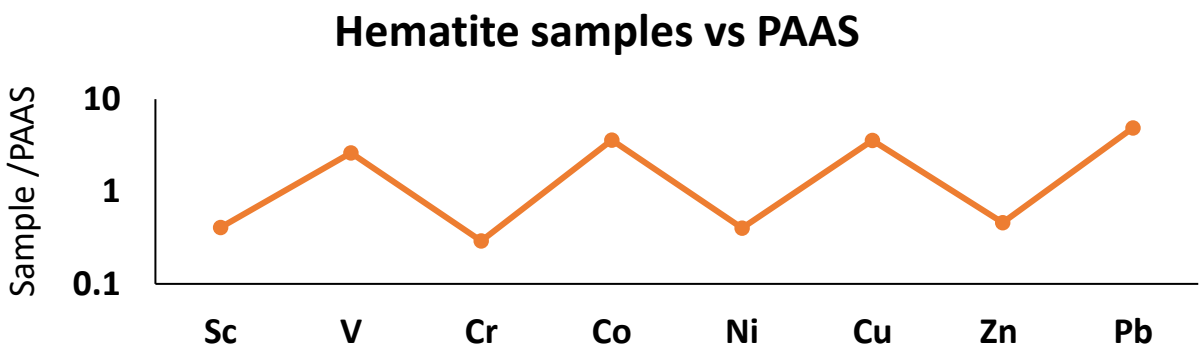

Figure 33. Average trace element abundances of hematite samples relative to Post Archaean Australian Shale (n=6).

With regards to transition metals, the hematite samples appear to be slightly enriched in vanadium, copper , cobalt and lead relative to PAAS, whereas nickel, scandium, chromium, and zinc are relatively depleted.

3.2.1 Quartzite

The Mapedi quartzites analyzed in this study are iron rich. Average iron oxide content for the quartzites is 16.69% with individual contents ranging from as low as 3.04% to as high as 40.64% iron oxide. These iron rich samples also tend to be enriched in the mineral aegirine as evidenced by their higher sodium oxide content. As a result, the average quartzite iron oxide and sodium oxide content is enriched relative to PAAS. Phosphate contents are also slightly enriched relative to PAAS.

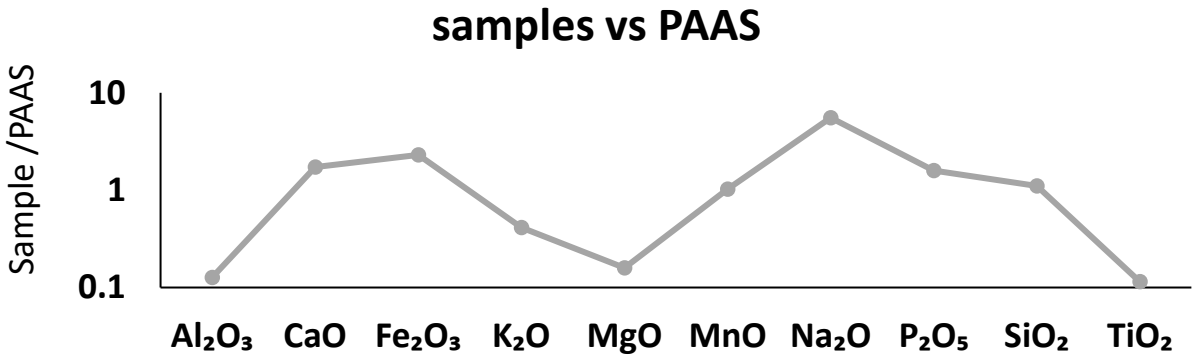

Figure 34. Average major oxide abundances of quartzite samples relative to Post Archaean Australian Shale (n=12).

In terms of REE geochemistry, the quartzites are considerably depleted relative to PAAS. Analysis of the samples produces a plot with a weakly positive slope, indicating a slight enrichment of HREEs relative to LREEs. There is also a weak positive Eu anomaly.

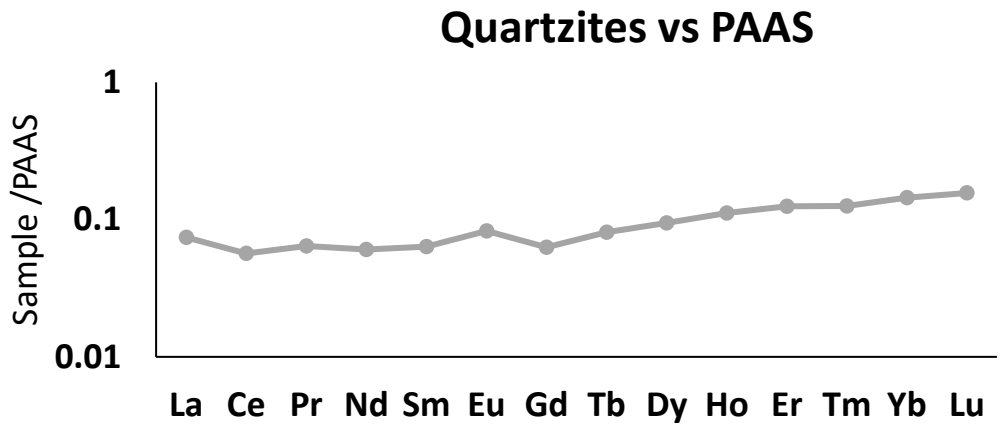

Figure 35. Average REE abundances of quartzite samples relative to Post Archaean Australian Shale(n=12).

The HFSE plot shows that these quartzites are also enriched in barium, strontium and to a lesser extent thorium relative to PAAS.

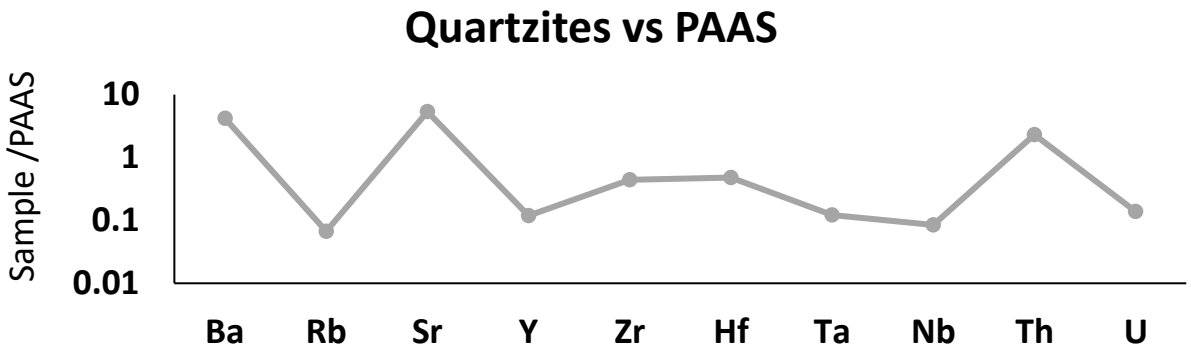

Figure 36. Average HFSE abundances of quartzite samples relative to Post Archaean Australian Shale(n=12).

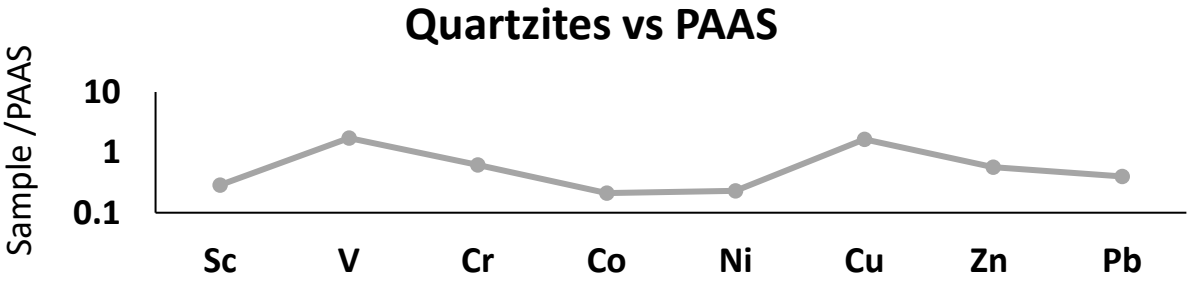

Figure 37. Average trace element abundances of quartzite samples relative to Post Archaean Australian Shale(n=12).

In terms of transition metal geochemistry, the quartzites are generally depleted relative to PAAS except for a slight enrichment in vanadium and copper.

3.2.2 Shale

Bulk oxide geochemistry results show that the shales analyzed in this study are enriched in iron oxide content relative to PAAS. As is the case with the other lithologies analyzed, the shales also show an enrichment in sodium oxide content relative to PAAS. There is also a depletion in MgO, MnO, K_2O, and CaO while Al_2O_3 behaves relatively more conservatively.

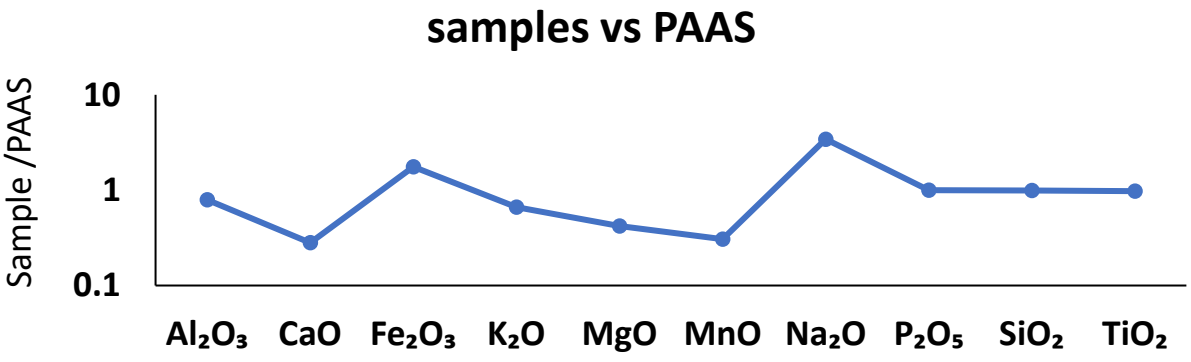

Figure 38. Average major oxide abundances of shale samples relative to Post Archaean Australian Shale(n=7).

REE geochemistry for the shales when plotted against PAAS shows a slight depletion in rare earth elements relative to PAAS as well as a weak negative slope indicating that there is an enrichment of LREEs relative to HREEs. The data also shows the presence of a weak Eu anomaly.

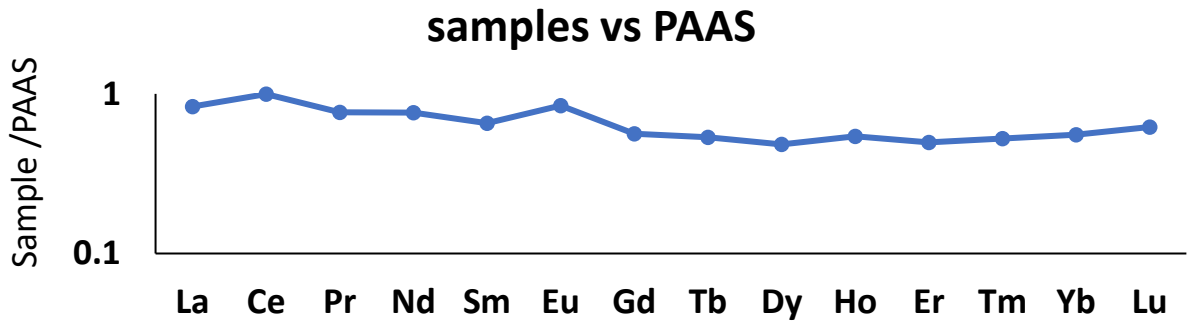

Figure 39. Average REE abundances of shale samples relative to Post Archaean Australian Shale(n=7).

In terms of HFSEs, within the shale samples there is quite some variation in HFSE content with some samples being relatively more enriched than others (see Table 4 in Appendix A) but on average the shales also show an enrichment in Ba, Th, and U. Rb, Sr, and Y are slightly depleted while Zr, Hf, Ta and Nb behave more conservatively relative to PAAS.

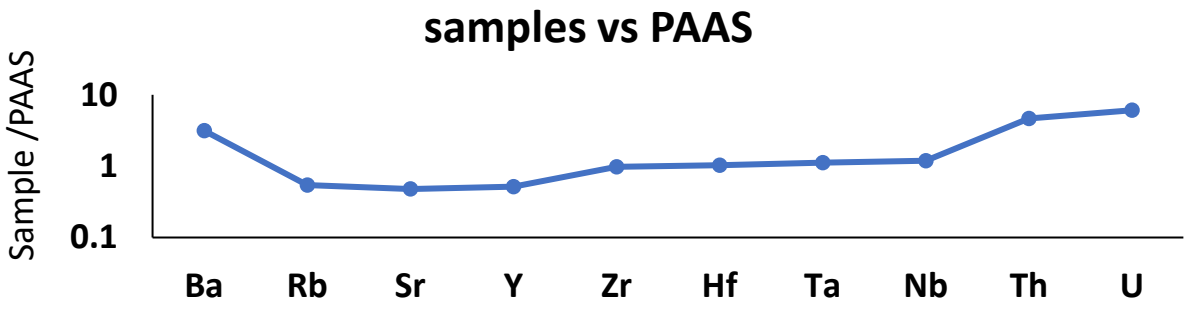

Figure 40. Average HFSE abundances of shale samples relative to Post Archaean Australian Shale(n=7).

Transition metal abundances within the shales relative to PAAS indicates an enrichment in vanadium and copper to a slighter extent. Co, Ni, and Zn are also slightly depleted.

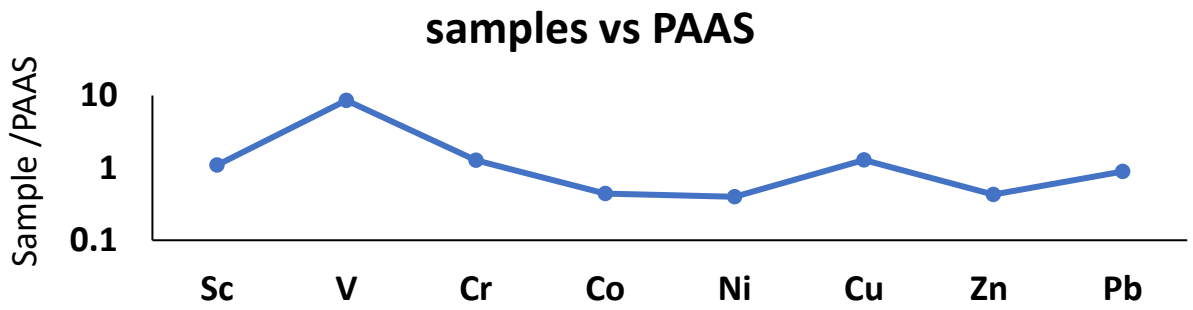

Figure 41. Average transition metal abundances of shale samples relative to Post Archaean Australian Shale(n=7).

4. DISCUSSION

4.1 Pre-metasomatic protoliths

4.1.1 Hotazel hematite-rich unit

What is obvious from observing the hand specimens of these rocks, as well as studying their geochemical make up is that they have been extremely altered. On the surface they look quite simple but their mineralogy and geochemistry across the studied stratigraphic length tell a more complex story. One issue which poses a challenge is that of exactly what primary lithology would have produced the massive hematite section observed at the top of the Hotazel Formation, where it comes in contact with the Mapedi Formation. The lithological succession of the Hotazel Iron Formation includes four units of BIF interbedded with three units of Mn-ore, where the Mn-ores have a transitional hematite-lutite facies flanking them on both sides (Tsikos & Moore, 1997). The formation is normally capped by the Mooidraai Formation dolomites (Tsikos *et al*., 2003), which are preserved as erosional relicts in the KMF (Tsikos & Moore, 1997). Based on the extensive erosion of the Mooidraai Formation as noted by Tsikos & Moore (1997) and as observed in the drill core sections described in this study, the dominant lithology expected to be observed at the contact would be Hotazel BIFs (more on this later). These BIFs may be those of the carbonate-rich facies, and could mark the transition into the Mooidraai Formation. However, this does not seem to be apparent when observing the samples which are found at the top of the Hotazel Formation in the analyzed drill core sections. These rocks are quite dense, brown to reddish in colour, and have a smooth, massive texture. They are hematite-rich, silica and carbonate poor, and they seem to have undergone extensive oxidation while largely maintaining a consistent fabric. There is also little evidence of pervasive leaching that would result in any kind of brecciation and volume loss which may indicate that they formed at the expense of a BIF protolith. Essentially, they bear little physical resemblance to Hotazel BIFs which are usually lighter in color, silica rich, and characterized by distinctive banding. Furthermore, they are also geochemically distinct from Hotazel BIF. This is based on the major element geochemistry of the hematite-rich samples obtained at the Hotazel-Mapedi contact which are characterized by a wide range in manganese content, with more than 30% manganese oxide in some cases. This poses a question as to what would have been the source of such an extreme enrichment if indeed these rocks are oxidized Hotazel BIF.

The most straightforward solution to this problem might lie in the possibility that perhaps at the Transvaal-Olifantshoek contact, it is not oxidized upper carbonate-rich BIF being intersected. It

could be the case that the unconformity cuts much deeper into the Hotazel Formation into the more manganese rich layers, possibly the transitional lutite facies sitting right below the upper BIF layer as shown in figure 3. This possibility could account for the high manganese oxide content found within these hematite rich samples.

Figure 42 shows a major oxide plot of the average of all hematite samples normalized against average pristine Hotazel BIF analyzed by Mhlanga(2020) (see appendix A). The Hotazel BIF were obtained from the Gloria mine area in the northern KMF (see figure 1). This plot shows that in terms of major oxide composition, the hematite-rich samples analyzed in this study are not geochemically consistent with average pristine Hotazel BIF .

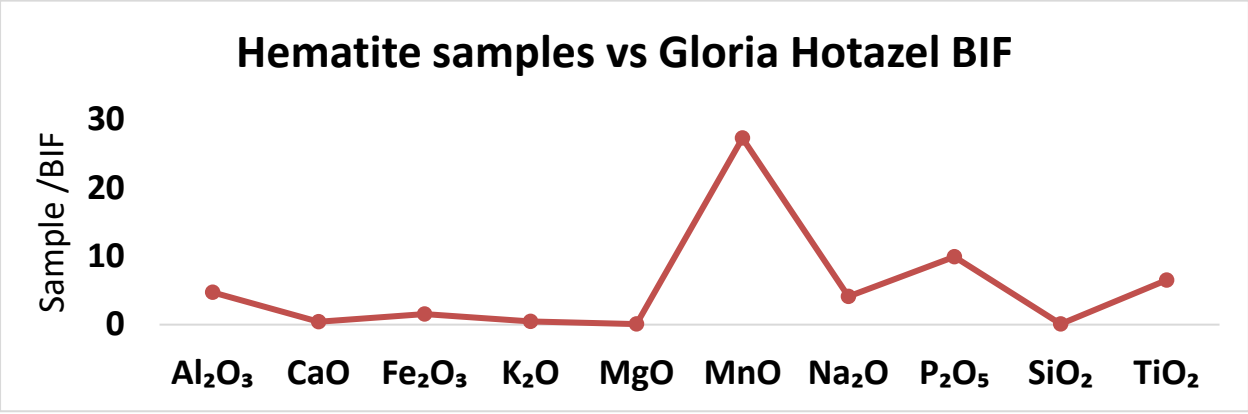

Figure 42. Average hematite sample normalized against Hotazel BIF from Gloria Mine(n=7).

Figure 43 shows a major oxide plot of the average of all hematite samples normalized against actual Hotazel BIF of borehole DB66 which was provided by the Hotazel Mine. The purpose of the plot is to compare the average major oxide composition of the hematite rich samples with that of average Hotazel BIF from core DB66 (see table 1).

Table 1. Major oxide abundances (in wt.%) for Hotazel BIF DB66.

	Al_2O_3	CaO	Fe_2O_3	K_2O	MgO	MnO	Na_2O	P_2O_5	SiO_2	TiO_2
DB66D	0.25	0.81	42.78	0.00	0.10	0.95	11.09	0.32	43.48	0.01
DB66E	0.13	0.78	46.91	0.00	0.11	0.71	10.34	0.33	40.88	0.00
DB66F	0.27	0.78	55.59	0.06	0.25	5.20	7.08	0.33	29.51	0.01
DB66H	1.73	0.44	61.94	0.93	1.98	2.15	4.80	0.20	24.42	0.03
DB66J	0.31	0.56	37.82	0.03	0.14	4.47	11.04	0.19	44.77	0.00
Average	0.54	0.67	49.01	0.20	0.52	2.70	8.87	0.27	36.61	0.01

The samples analyzed from core DB66 have been altered by sodic metasomatism, hence they are not suitable for reference as a possible protolith like in the case of the Gloria Mine BIFs. However,

they do provide some insight into what BIFs of the same formation in the same geographical area might present as geochemically after having undergone sodic metasomatism.

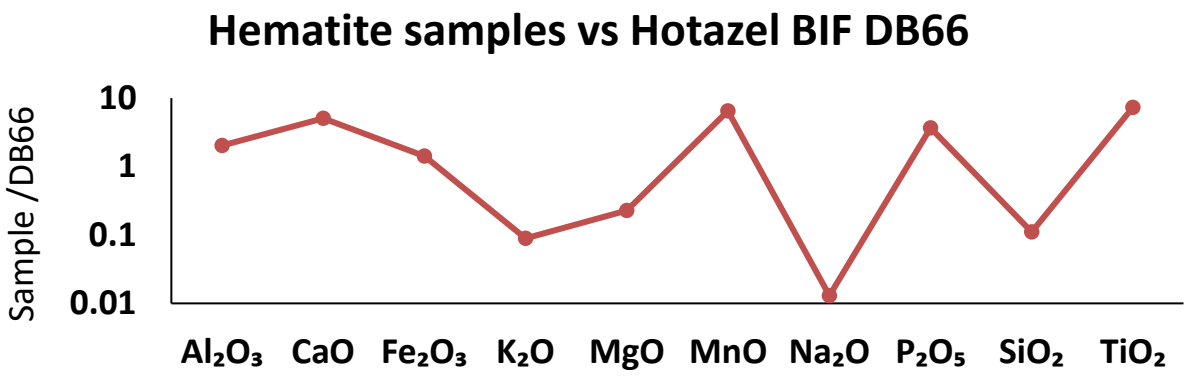

Figure 43. Average hematite sample normalized against Hotazel BIF DB66(n=7).

The plot shows that the hematite samples analyzed in this study are also not consistent with sodic-metasomatized Hotazel BIF in terms of bulk rock composition. Besides the substantial difference in manganese content, the severe depletion in sodium content in the hematite samples relative to drill core DB66 is quite noteworthy. This is becasuse Tsikos and Moore (2005) have reported sodic metasomatism (in the form of aegirine enrichment) in BIFs of the Hotazel Formation (around Wessels and N'chwaning (see figure 1)) and the BIFs of core DB66 also show this characteristic aegirine enrichment. Thus, even though the hematite samples have been impacted by sodium rich metasomatic fluids that resulted in the formation of sugilite and aegirine in the quartzites right above them, as well as aegirine in the BIFs in the same area (as observed in core DB66), these fluids failed to produce sodium enrichment in the form of aegirine within the hematite samples themselves. This likely means that these rocks must have originally been very silica poor prior to the sodic metasomatism, unlike the Gloria Mine Hotazel BIFs or the DB66 BIFs. This could also be the reason why silica rich minerals were not formed in the hematite-rich samples.

Table 2 shows assay results for transitional lutites from borehole DB89 and W351, these assay results were also provided by the Hotazel Mine. These holes were sources of some of the drill core samples analyzed in this study. The transitional lutite samples are about 2 m away from the Traansvaal-Olifantshoek contact, where the hematite-rich samples analyzed in this study were obtained.

Table 2. Major oxide abundances (in wt.%) for Hotazel lutite samples from drill cores DB89 and W351.

	Al_2O_3	CaO	Fe_2O_3	K_2O	MgO	MnO	Na_2O	P_2O_5	SiO_2	TiO_2
DB89	0.31	3.33	30.11	0.02	0.10	32.45	0.12	0.01	6.33	0.02
W351	0.17	1.62	44.37	0.02	0.11	22.37	0.12	0.01	3.06	0.02

Figure 44 shows a similar major oxide plot of the hematite samples, this time normalized against transitional lutites from borehole DB89 and W351 (table 2). The purpose of the plot is also to compare the major oxide composition of the hematite samples with that of transitional lutites from the Hotazel Formation. These results compare much more consistently with the hematite samples analzed in this study, especially in terms of the manganese and sodium oxide content.

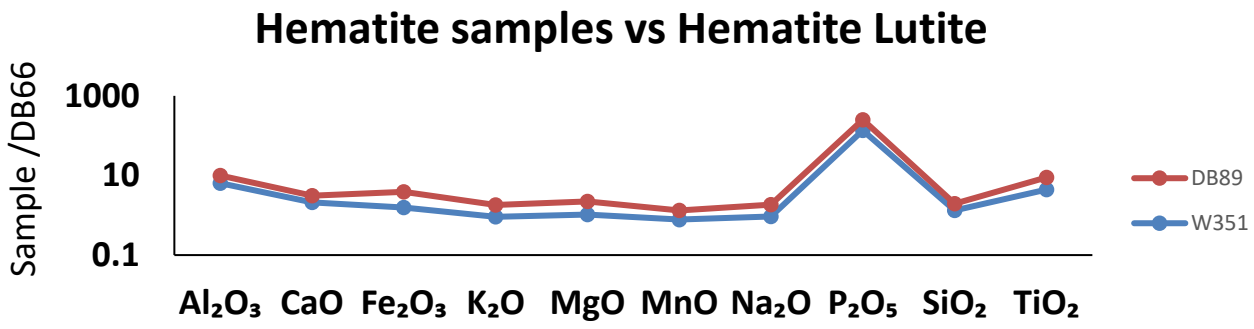

Figure 44. Average hematite sample normalized against Hotazel lutite samples from drill cores DB89 and W351(n=7).

Phosphate and titanium oxide contents of the hematite samples found at the contact seem to be quite high relative to the lutites further down the stratigraphy. This is likely related to the metasomatism occuring at the Transvaal-Olifantshoek contact, leaving a relatively cryptic fingerprint in this particular lithology due to its silica-poor nature.

Another interesting point that could shed more light into the possibility that these hematite-rich samples are likely transitional lutites lies in the trace element geochemistry of these rocks. Lutites from the Hotazel Fm in the Gloria Mine area further to the north are characterized by higher Co concentrations than the associated BIFs and Mn ores (Mhlanga, 2021), see appendix A for bulk rock values. Mhlanga (2021) described the average Co concentration in the Hotazel BIFs as very low, with values increasing significantly towards the manganese-rich assemblages. In the study, he showed that even though Co tended to concentrate in manganese-rich layers, peak Co

concentrations actually occur in the hematite-lutite transitions and not in the manganese ore layers themselves.

It highlighted that ultimately the Co concentrations were mostly controlled by hematite concentrations, thus Co formed in higher abundances in manganese-rich layers where hematite was relatively enriched and this is why peak Co values tended to occur in the more hematite-rich transitional lutites than in the Mn-ores, providing a way to further geochemically distinguish between the two in terms of a likely protolith for the hematite-rich samples found at the Transvaal-Olifantshoek contact.

The Gloria mine hematite-lutites record average Co concentrations of 50.29 ppm, whereas the manganese layers record a lower average of 40.78 ppm (see Appendix A). The Co concentration in the Gloria BIF layers is comparably lower recording an average of 3.87 ppm. In contrast, the hematite-rich rocks found at the Transvaal-Olifantshoek contact record an average Co concentration of approximately 83 ppm with the peak value reaching 174 ppm.

For comparison, this value is also consistent with assay results of transitional lutite located 2 m away from the Transvaal-Olifantshoek contact which record Co values of 167 ppm and 168 ppm respectively for cores DB89 and W351 (see appendix A). Correlation between manganese oxide abundance and Co enrichment within the hematite-rich samples of this study is established in the next section. This relationship is illustrated in the form of a correlation plot (see top left plot in figure 47) which shows a strong correlation between the two species, similar to what was proposed by Mhlanga (2020). Thus, it is quite evident that the pre-metasomatic protolith of the hematite-rich rocks found at the Transvaal-Olifantshoek contact is not Hotazel BIF and most likely hematite-lutite.

Again, this likely explains why minerals like sugilite, and aegirine did not form within the lutites themselves, despite being iron and manganese rich. There simply was no silica available up until the fluid got in contact with the Mapedi quartzites which contain approximately 69% silica with peak abundance sitting at approximately 96%.

Having established hematite lutite as the likely lithology found at top of the Hotazel Formation (at the Hotazel-Mapedi contact), it is more apparent that at the transition between the Transvaal and the Olifantshoek, there is hematite-lutite of the Hotazel Foemation is coming in contact with iron rich quartzites and shales of the Mapedi Formation.

4.1.2 Mapedi quartzite and shale

The Mapedi quartzites located in the southern part of the basin (Postmasburg) record average silica concentrations of about 88 wt% (Monku, 2016). By comparison, the northern Mapedi quartzites located in the Hotazel Mine area are relatively less enriched in silica. The reason for this lies in their iron oxide content relative to the Postmasburg quartzites. The average hematite content of the Postmasburg quartzites is approximately 7 Wt. % (see Appendix A) whereas their more northern counterparts record an average hematite concentration of 17 Wt. %. Thus, while the northern quartzites are classified as quartzites by virtue of the fact that they form part of the wider Mapedi Formation which traditionally boasts quartzite lithologies containing just silica and not much of anything else, metasomatism and oxidative processes possibly transformed the northern quartzites in this study to much more iron rich versions of their protoliths and in some cases where these rocks record up to 40 Wt. % hematite concentration, they may no longer even classify as quartzites in a strict geochemical sense.

The Mapedi shales show features of oxidation similar to those observed across the Traansvaal-Olifantshoek contact, in that they are enriched in iron. However their oxidized nature is a feature reported in much earlier studies by Yamaguchi and Ohmoto (2006). They reported that hematite, the pigmenting agent of the red shales, was probably formed during the lateritic weathering of source rocks approximately 2.2 Ga ago, rather than by the modern oxidation/weathering of pre-existing Fe^{2+}-bearing minerals in the shales. Thus, compared to the quartzites, their iron enrichment possibly predates the likely sodic metasomatism that subsequently altered their geochemistry. However, relative to the quartzites, their geochemical composition seems more on par with results from geochemical studies of their unweathered protolith from the study of Yamaguchi and Ohmoto (2006), except for the fact that the red shales have a strong sodium enrichment relative to their protolith, just like the quartzites stratigraphically below them. It is worth noting that on average, quartzites from the southern part of the basin in Postmasburg, have sodium oxide content that is below detection limits (Monku, 2016). Thus, within the Mapedi Formation observed in the south, sodium oxide content is extremely low and mostly undetectatble, especially within the quartzites. Therefore, geochemical results obtained from the northern Mapedi quartzites and shales (from the Hotazel mine area) in this study show clear evidence that there has been a secondary introduction of sodium into the Mapedi, and this created conducive conditions for the formation of minerals such as sugilite and aegirine amongst others within the quartzites as well as albite within the red shales.

4.2 Metasomatic geochemical fingerprint

4.2.1 Hotazel hematite-rich unit

By comparing the geochemistry of the samples in this study with samples of the same formation which are from other parts of the KMF, it is possible to get insight into the geochemical fingerprint which the metasomatic fluid would have left on these rocks.

In the case of the hematite-rich samples, they have been proposed to most likely be altered lutite. And in this case, the geochemical fingerprint left on these hematite-rich samples as a result of the metasomatic process is relatively cryptic compared to the quartzites which show a clear secondary addition of sodium oxide leading to the formation of certain sodium minerals such as sugilite and aegirine.

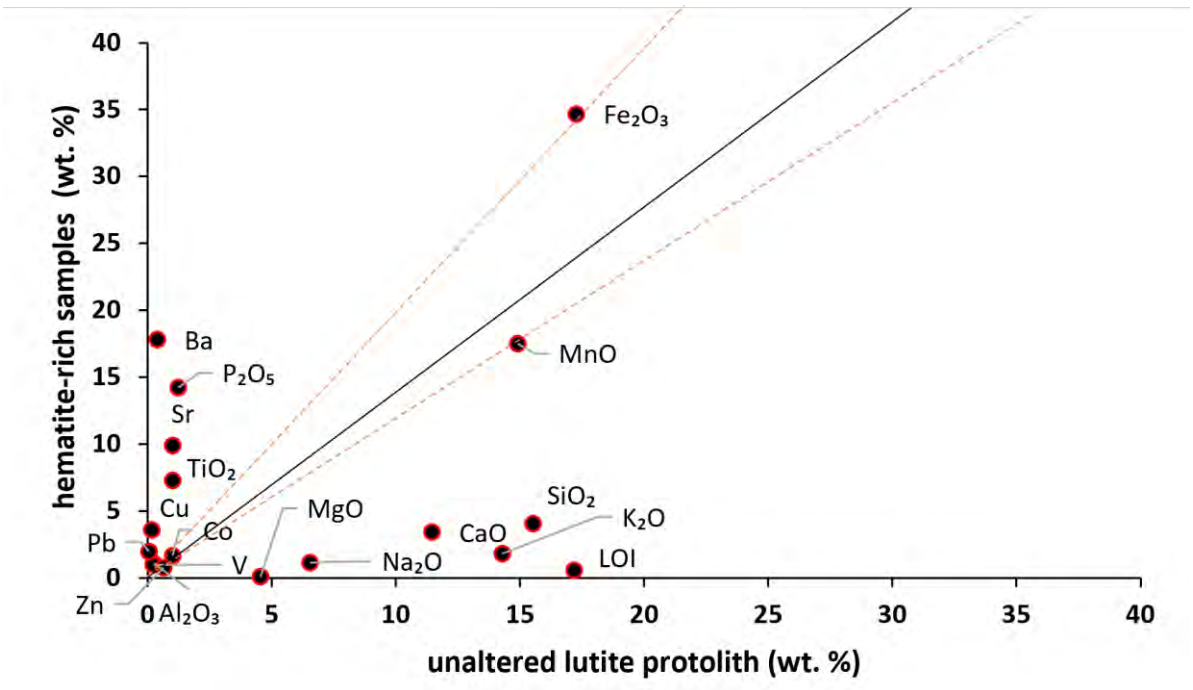

Figure 45. Isocon diagram of altered ferruginous hematite samples versus an unaltered lutite protolith from Gloria mine.

An isocon diagram (figure 45) is used here to illustrate the effects of metasomatism in these rocks. The isocon diagram is useful in estimating the changes in mass, volume, or element concentration during metasomatic mass transfer processes (Grant (1986) ; Grant (2005)). To demonstrate this,

the isocon diagram shows a plot of the original unaltered rock (lutite protolith) against the altered rock (hematite-rich samples) (Grant (1986) ; Grant (2005)).

The chosen protolith used in the plotting of this isocon is lutite also obtained from the Gloria mine and studied by Mhlanga (2020) (see appendix A for bulk rock abundances). The reason for using the Gloria mine lutite as a protolith as opposed to the Hotazel lutite located 2 m away from the contact, is because the Gloria mine lutite is pristine and unaffected by modern weathering processes thus making it an appropriate protolith for the lutite located at the unconformity contact.

The isocon diagram is characterized by a 1:1 positive correlation reference line, which is the line of constant mass and represents the rock plotted against itself without any alteration. The field delineated by the red dashed lines is the field of immobility and is defined by the immobile species. These are elements or oxides that are presumed to be most conservative during the alteration process. The rationale behind defining a field of immobility rather than using specific immobile elements/oxides to define an isocon is because Al_2O_3 is likely mobile within the system and thus defining an isocon in this case might prove challenging. The field of immobility is therefore defined by two endmember isocons (Fe_2O_3 and MnO). The two end members were chosen because they are the major species that make up the Hotazel Formation and the field of immobility can be used to display what is enriched above and below the field that these two endmembers define. All species were converted to weight percent and scaled to achieve a more spread-out, visual representation (see appendix A for bulk rock values and scaling factors). Species plotting above the field of immobility depict gain during the alteration and those plotting below it depict a loss (Grant, 2005). Relative to the field of immobility defined by the endmembers, species such as SiO_2, CaO and K_2O are depleted in the altered lutite when compared to the unaltered protolith. Furthermore, species like MgO and Na_2O are almost completely removed during alteration.

On the other hand, there is a substantial enrichment in a variety of species such as P_2O_5, TiO_2, Ba, Sr, and Cu. Figure 44 shows that even when normalized against Hotazel lutite from the same borehole, just 2 m away from the Hotazel-Mapedi contact, the altered lutite at the contact still shows relative enrichment in Al_2O_3, P_2O_5, and TiO_2 compared to its counterpart 2 m deeper. This indicates that the enrichment in these oxides, particularly phosphates, is a characteristic feature of the metasomatism that is occurring at the contact between the Hotazel and Mapedi Formations.

Thus, with regards to the ferruginous lutite, the isocon shows that the impact of the metasomatism was predominantly oxidation and leaching of silica and carbonate. This possibly led to enrichment in hematite. There was also the addition of a variety of species including elements such as Ba, Pb, Sr, in the form of minerals such as baryte, banalsite, stronalsite, as well as the addition of phosphates in the form of apatite minerals. The enrichment of elements such as Cu, Zn, V, Co, and Mo indicate that this metasomatic fluid was a highly oxidized, sulphate bearing, phosphate rich, alkali rich brine which was able to effectively mobilize metals.

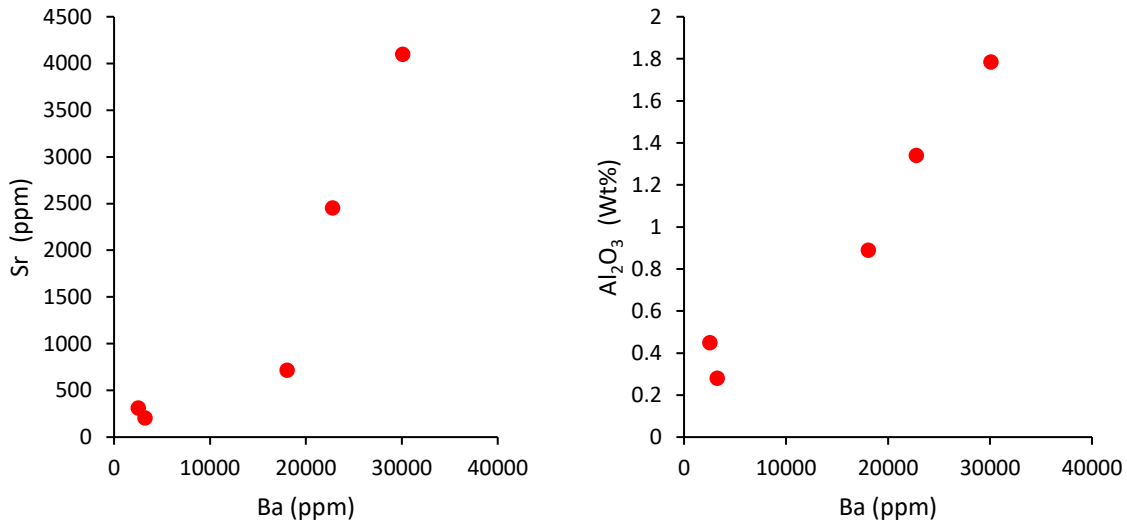

Figure 46. Correlation plots of barium versus strontium and aluminum oxide within ferruginous lutite samples.

Figure 46 shows correlation plots for barium vs strontium and aluminum oxide within the ferruginous lutite samples. There is a strong, positive correlation between barium and these two species. This is likely as a result of strontium substituting for barium in the mineral baryte, thereby forming the celestine endmember. As previously stated, in the case of aluminum oxide, its strong correlation with barium is most likely because it is incorporated into the barium mineral banalsite. It is also worth noting that strontium also substitutes for barium in banalsite, forming the stronalsite endmember.

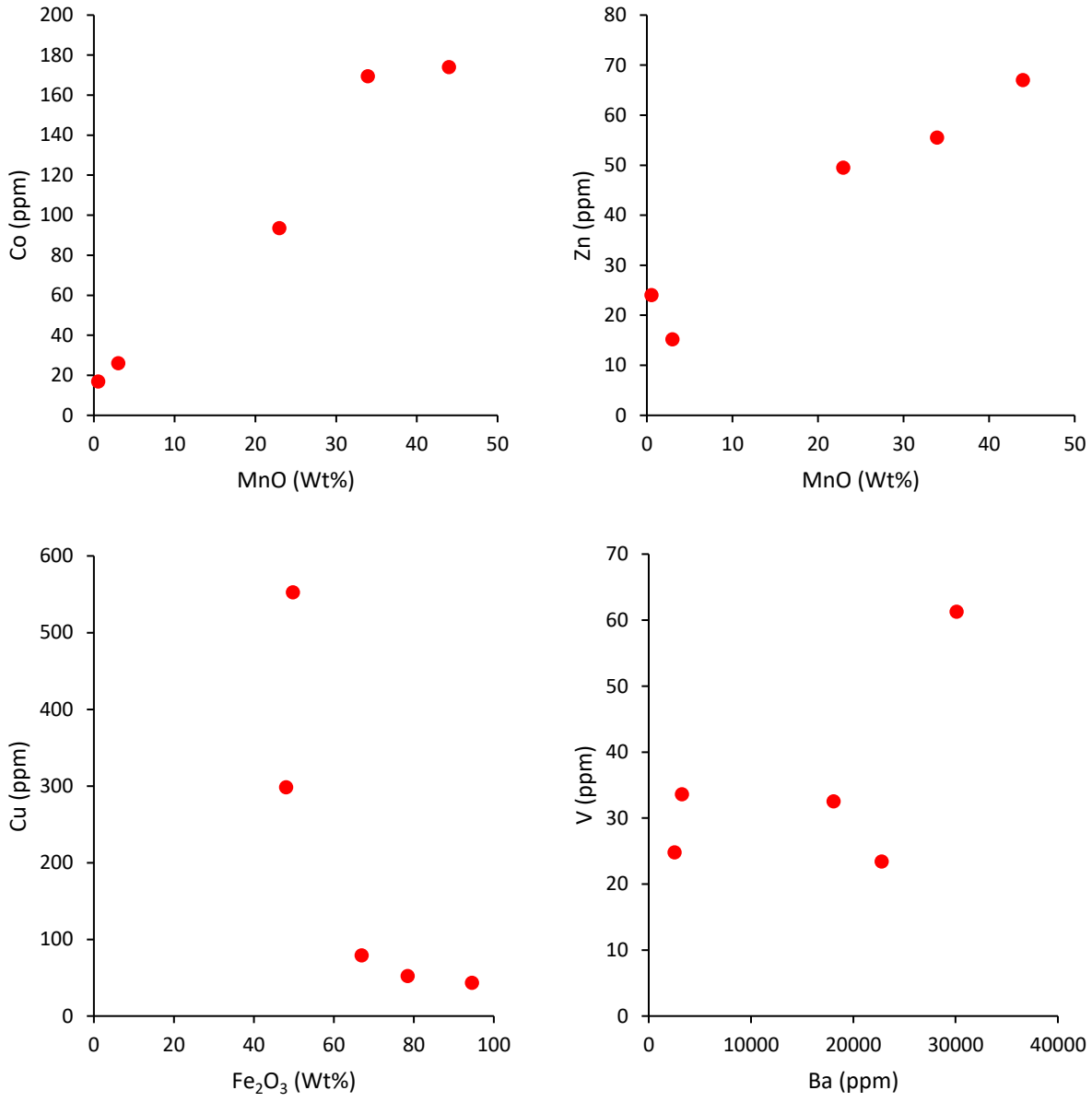

Figure 47. Correlation plots of iron and manganese oxide as well as barium versus various metal species within the ferruginous lutite samples.

Figure 47 shows more correlation plots. The top plots show a correlation of manganese oxide vs cobalt and zinc. There is also a strong, positive correlation between these species. As previously stated, cobalt tends to be absorbed extensively by hematite rich manganese bearing rocks such as the ferruginous lutite. Zinc also correlates with manganese oxide; this could be as a result of the oxidized fluid depositing trace amounts of zinc, arguably as some sort of oxide mineral such as zincite which incorporates Mn into its mineral structure.

The bottom left plot shows the relationship between hematite and copper. There appears to be a negative correlation between hematite and copper within the lutite samples. In the bottom right

plot, there is a weak, positive correlation between barium and vanadium. It is likely that vanadium is occurring in trace amounts in association with a barium mineral but may also be occurring in association with another oxide mineral thus its concentration is not strictly controlled by barium.

4.2.2 Mapedi quartzite and shale

With regards to the quartzite and the metasomatic imprint left on them by the fluid, the features of the alteration are relatively less cryptic compared to the lutite. Figure 48 shows a plot of Mapedi quartzites from the northern Hotazel mine normalized against Mapedi quartzites from the southern Postmasburg. This plot also shows an enrichment in phosphates in the Mapedi quartzites from the Hotazel area relative to those from Postmasburg. Thus, this strengthens the possibility that the metasomatic fluid responsible for the alteration observed at the Hotazel-Mapedi contact was not only sodium-rich but also phosphate-bearing.

This possibility is supported by the abundance of Sr-rich apatite identified right at the contact between the two Formations (see figures 22 and 23). Moderate enrichment in Al_2O_3 relative to the lutite protolith possibly explains the appearance of albite, banalsite and stronalsite at the lutite-quartzite contact where Al_2O_3 could easily be mobilized to react with the overlying quartzites to form alkali rich minerals (see figures 20, 21 and 23).

On a macroscale, these rocks are characterized by secondary features such as their striking purple as well as green-colored tint and in some sections. The evidence of pervasive oxidation and hematite enrichment is very extensive (see figure 10). Thus, within the quartzites, the characteristic feature of metasomatism is the development of secondary sodium-rich minerals. The reason for this is because as previously discussed, Mapedi quartzites from Postmasburg have sodium oxide content below detection limits (see appendix A). Therefore, the presence of sugilite and aegirine within the quartzites from the Hotazel Mine area is anomalous and certainly of secondary origin.

Figure 48 demonstrates this visually. It compares northern Mapedi quartzites (from the Hotazel Mine) to southern Mapedi quartzites (from Postmasburg) and shows that relative to the Postmasburg quartzites, the quartzites in this study show a substantial spike in sodium oxide content. Furthermore, there is also an enrichment in calcium oxide, potassium oxide, phosphate, manganese oxide as well as iron oxide content.

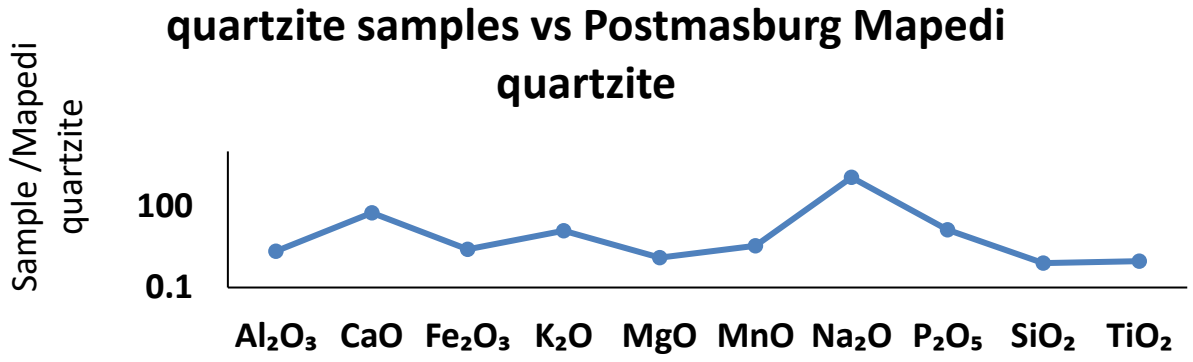

Figure 48. Average major oxide concentrations of Hotazel Mine quartzite from the Hotazel-Mapedi contact normalized against Postmasburg Mapedi quartzite (Table 8 (Appendix A)).

The spike in iron oxide content is consistent with the physical evidence of pervasive oxidation and hematite enrichment observed in drill core hand samples. The substantial loss in alkali oxides within the lutite as shown in the isocon diagram in figure 45, coupled with the enrichment in alkali oxides within the quartzites further indicates that the metasomatic hydrothermal alteration impacting the rocks at the Hotazel-Mapedi contact is characterized by alkali mobilization.

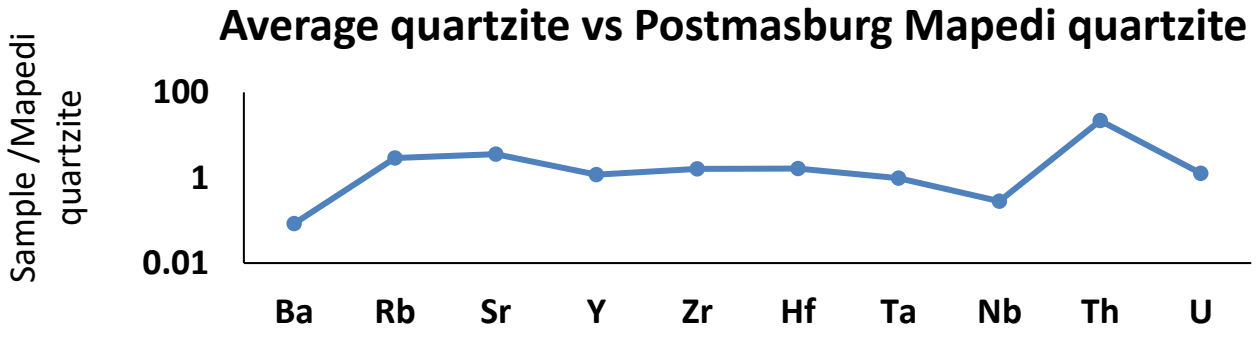

Figure 49. Average HFSE concentrations of quartzite from the Hotazel-Mapedi contact normalized against Postmasburg Mapedi quartzite (Table 9 (Appendix A)).

Figure 49 also shows another comparison between the northern and southern quartzites in terms of HFSE concentration. The northern quartzites in this study also show an enrichment in thorium. Relative to the southern Mapedi quartzites, the northern quartzites appear depleted in barium. Though barium concentration within the northern quartzite is highly variable, as is also the case in the south, nevertheless they are still substantially enriched in barium with an average concentration of approximately 1398 ppm and the highest concentration reaching approximately 11469 ppm. For comparison, southern quartzites record an average barium concentration of approximately 16585 ppm. Thus, the reason for the deficiency of barium relative to southern quartzites is because

southern quartzites have been reported to be extremely and anomalously enriched in barium as a result of metasomatism (Monku, 2016). The possible relationship between the metasomatism reported in the southern quartzites and the metasomatism observed in the northern quartzites will be discussed later.

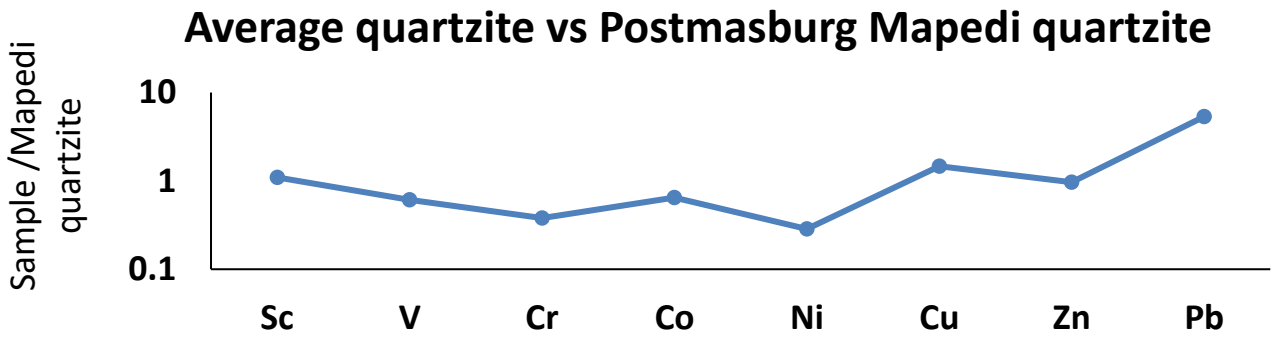

Figure 50. Average transition metal concentrations of quartzite from the Hotazel-Mapedi contact normalized against Postmasburg Mapedi quartzite (Table 9 (Appendix A)).

Figure 50 also shows that relative to southern Mapedi quartzite, northern Mapedi quartzite is enriched in lead. Thus, with regards to the quartzites, metasomatism seems to have resulted in oxidation, alkali enrichment leading to the formation of minerals such as sugilite, aegirine, and albite to a lesser extent, as well as an enrichment in lead, like what is observed in the ferruginous hematite-rich rocks.

Figure 51 shows correlation plots of iron oxide vs sodium oxide as well as the sum of iron and manganese oxide vs alkali oxides. The strong, positive correlation between iron oxide and sodium oxide is consistent with the presence of aegirine within the quartzites. The second plot shows a strong positive correlation between the alkali oxides and iron and manganese oxides within quartzites and this is consistent with the presence of sugilite.

It is worth noting that there are some outlier points that occur as a result of alkali oxide concentration possibly being controlled by another alkali rich mineral, in addition to albite, aegirine and banalsite, possibly a mica.

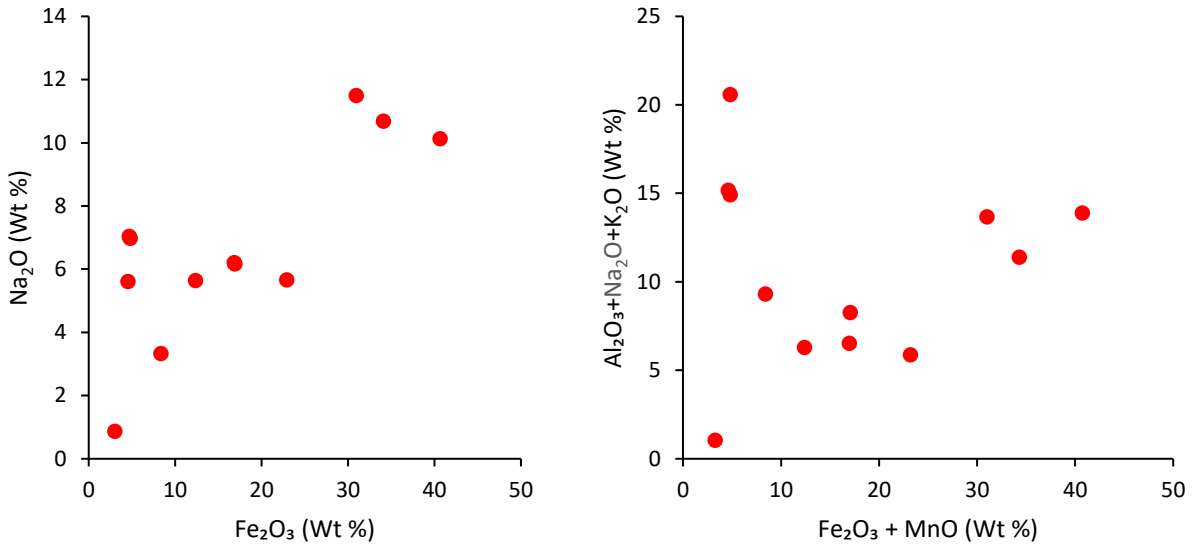

Figure 51. Correlation plots of iron and manganese oxide versus alkali oxides within northern Mapedi quartzites.

Thus, the outliers occur because alkali concentration is not strictly controlled by the presence of sugilite.

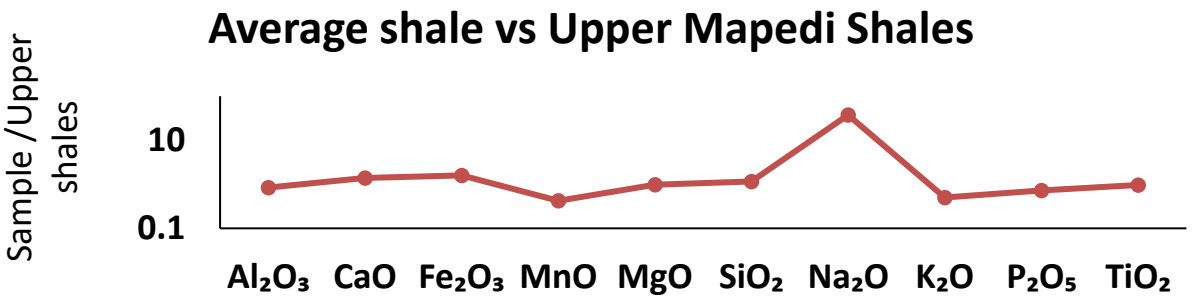

Figure 52. Average major oxide concentrations of shale from the Hotazel-Mapedi contact normalized against average upper Mapedi shales studied by Yamaguchi and Ohmoto (2006).

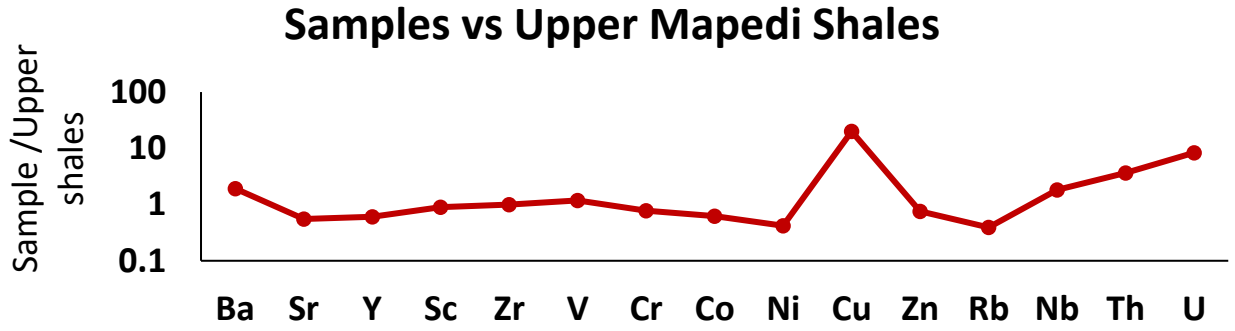

Figure 53. Average trace element concentrations of shale from the Hotazel-Mapedi contact normalized against average upper Mapedi shales studied by Yamaguchi and Ohmoto (2006).

Figures 52 and 53 show plots of the Mapedi red shales analyzed in this study normalized against unweathered Mapedi red shales studied by Yamaguchi and Ohmoto (2006). Based on the two plots, it is possible to infer the effects of metasomatism within the red shales. In the case of the red shales, just like the quartzite, metasomatism is characterized by a substantial enrichment in sodium oxide as shown in figure 52, particularly in the form of the mineral albite as confirmed by SEM analysis (see figure 20). There is also an enrichment in copper, thorium, and uranium as well as barium to a lesser extent, possibly in the form of banalsite. Albite occurs more predominantly within the shales compared to the quartzite for the same reason that there is no aegirine within the lutite, the minerals that are formed as a result of the metasomatic fluid are partly controlled by the lithologies encountered by the fluid. The lutite has negligible silica, thus baryte, phosphate and metal oxide enrichment predominate within that lithology. Once the alkali rich brine came in contact with the quartzite unit however, it was able to form alkali rich silicates because of the abundance of silica. There was possibly also some mobilization of iron and manganese from the underlying lutite unit which allowed minerals like sugilite (likely a more iron rich endmember), and aegirine to form along with minerals such as albite, banalsite, stronalsite as well as pectolite and andradite to a much lesser extent. On encountering the alumina rich shales, the predominant mineral formed is albite (in much higher concentrations than in the quartzite) and possibly banalsite to a lesser extent.

4.3 Structural and stratigraphic controls on metasomatism

As previously stated, the Kalahari Manganese Field is characterized by thrusting and faulting as a result of the Kheis and Kibaran orogenies. These structural events, particularly the Kibaran orogeny, have been described as having been essential for the subsequent 'Wessels' hydrothermal event which upgraded the manganese ore in the north western part of the KMF. Early models put forward by Beukes *et al*. (1995) as well as Gutzmer and Beukes (1995) for the genesis of high-grade Mn ore in the northern KMF proposed a single, major event of hydrothermal fluid flow along faults and pervasive leaching of manganese ore laterally away from fault zones, followed by volume loss, compaction, and residual Mn enrichment (Gutzmer and Beukes, 1997) . These models point to the abundance of normal, north-south–trending faults which are known to cross-cut the Hotazel and Mapedi Formations (see figure 1) as the pathways by which hydrothermal fluids

propagated during the hydrothermal upgrading of the northern KMF. To summarize, hydrothermal alteration was described as a single fluid event that was largely fault-controlled.

However, a study by Tsikos *et al*.,(2003) suggested that hydrothermal alteration and metal enrichment in the northern KMF may not solely be attributed to pre-existing faults and that the role of the Hotazel-Mapedi unconformity surface as a major conduit for fluid flow is likely underestimated. Their study highlighted the effects of pervasive oxidation, carbonate leaching, and residual metal enrichment in the uppermost portions of the Hotazel Formation, and dolomitization and incipient oxidation at an adjacent, stratigraphically lower position. It pointed out that at deeper stratigraphic levels, away from the unconformity surface, the Hotazel Formation rocks remained relatively unaffected by these processes.

In the study by Tsikos *et al*.,(2003), it was also suggested that mineralogical evidence from the northern Kalahari Manganese Field, such as the diversity of mineral species found in veins, vugs, along fault zones, and at specific stratigraphic intervals of the Hotazel Formation likely implied a multistage fluid-rock interaction history, rather than a single hydrothermal event. This possibility of a multi-stage fluid event was subsequently revisited in a study by Tsikos and Moore (2005) where the necessity of Hotazel BIF containing essentially quartz and hematite in order to form aegirine was invoked. Based on the need for such a rock precursor, the study proposed that it was likely that prior to the sodic metasomatic event, the Hotazel rocks had already undergone thorough oxidation, carbonate leaching and residual enrichment in higher oxides of Fe and Mn, possibly due to low-temperature, unconformity- related fluid-flow processes.

This possibility of prior oxidation before sodic metasomatism is relevant to the aim of this study because it may explain the features observed in the lithologies at the contact such as the extensive oxidation of the northern Mapedi quartzite relative to the southern Mapedi quartzite as well as the metal enrichment of the lutites. If the prior oxidation model is accurate, iron enrichment within the Mapedi would have allowed for the formation of aegirine and iron rich sugilite. This does not necessarily mean that the sodic fluid was not mobilizing iron. However, it possibly means that the iron enrichment of the quartzites need not be extensively attributed to the sodic metasomatic alteration, and that the fluid likely encountered an already substantially oxidized quartzite unit which it exploited in order to produce the iron-rich, sodic mineral assemblages observed within the northern Mapedi quartzite.

The same can be inferred for the lutite, the possibility of a multi-stage metasomatic event could mean that metal enrichment occurred prior to the sodic metasomatism which more likely

predominantly involved relative enrichment in barium and phosphate. The reasoning behind this lies in the fact that in the drill cores analyzed in this study, the key distinction between the lutite at the Hotazel-Mapedi unconformity and the lutites just 2 m further down the stratigraphy is not necessarily a substantial difference in metal enrichment but the substantially high barium content as well as relatively higher phosphate content. Thus if the possibility of a multi stage hydrothermal event is invoked, it would mean that oxidation, carbonate leaching and metal enrichment predominantly occurred prior to the enrichment in barium and phosphate. It is important to highlight again that this does not mean that other metals could not have also been mobilized during sodic metasomatism, it only suggests that, where the lutite is concerned, this was possibly not the predominant feature of the sodic alteration occuring at the unconformity contact.

Furthermore, the occurrence of barium and phosphate enrichment in the lutite at the contact relative to stratigraphically deeper lutite, coupled with the consistent occurrence of sugilite and aegirine occurring close to the Hotazel-Mapedi unconformity contact (see figure 15) possibly highlights the importance of the unconformity contact as a major conduit for fluid flow, allowing the phosphate and barium bearing, alkali-rich brine to be focused along the contact, laterally propagating itself as it reacted with the lithologies it encountered and subsequently producing the mineral assemblages observed at the contact between the two formations. If indeed it is the case that the unconformity played a major role in the sodic alteration, it means the fluid is not only exploiting the unconformity and reacting with the rocks it encounters, but could also be progressively obscuring the original unconformity where these two formations originally met. If this is true, then the Olifantshoek-Transvaal unconformity may need to be reinterpreted and re-characterized.

4.4 Comparison with the broader KMF region

Having established the occurrence of an alkali-rich mineral assemblage characterized predominantly by the presence of minerals such as sugilite, aegirine, banalsite, baryte, apatite, albite, pectolite, and andradite at the contact between the Hotazel and Mapedi Formations, it is worth noting that such minerals have been widely reported in other parts of the KMF. The secondary nature of the minerals described in this study has been established by the presence of cross-cutting quartz veins as well as geochemical comparisons with unaltered protoliths and samples from other parts of the KMF. As previously stated, in the northern Wessels/Black Rock

area, a variety of rare silicate minerals including andradite, pectolite, and sugilite have been reported along with aegirine (Dixon, 1985; Gutzmer & Beukes, 1996). Sugilite has also been reported in the PMF by Moore *et al*.(2011), in the Wolhaarkop breccia where it occurs in association with braunite, albite, K-feldspar and aegirine. Moore *et al*.(2011) also reported sugilite displaying a fibrous texture, a feature also observed within the sugilite bearing quartzites analyzed in this study. Aegirine has also been reported to occur in the BIFs of the Hotazel Formation by Tsikos and Moore (2005). In addition to these, baryte-rich mapedi quartzites have been reported in the Postmasburg area by Monku (2016), at the contact where the Ongeluk lavas are thrusted over the Olifantshoek. Costin *et al*. (2015) also reported the presence of Ba- and V-rich phases in the form of baryte and tokyoite. Thus, it is quite clear that there is a common thread between the different regions of the KMF where metasomatism has been observed, studied and characterized. In the north-western KMF at Wessels, in the north-eastern KMF at Hotazel, and in Postmasburg, alkali metasomatism has been reported and this hydrothermal alteration has been characterized consistently by the predominance of aegirine along with minerals such as sugilite, baryte, albite, amongst others. The geochemical parallels occuring across these regions of the KMF could be pointing to the possibility of widespread, large scale, alkali metasomatism by a predominantly Na-rich basinal brine(s) that is interacting with the different rock packages and producing mineral assemblages in accordance with the lithologies it encounters as well as in accordance with the fluid's own chemistry, thereby creating a variety of mineral assemblages as it exploits structural features such as faults and fractures and in the case of this study, the Transvaal-Olifantshoek unconformity whose adjacent relationship with the observed alkali-rich mineral assemblage points to the possibility of it being a major conduit for fluid propagation. This metasomatic event likely postdates a previous fluid event that resulted in pervasive oxidation of the lithologies at the Hotazel-Mapedi contact. The metasomatic fluid(s) responsible are likely connate and could have been produced as a result of the thrusting and burial processes that occurred during the Kheis orogeny during which the Black Ridge thrust was propagated from north to south of the KMF, where the Voelwater rocks i.e. the Hotazel Formation was thrusted over the Olifantshoek in the north, and the Ongeluk Formation was thrusted over the Mapedi Formation in the south.

5. CONCLUSIONS

5.1 Conclusions

This study submits evidence for the case of regional-scale alkali metasomatism in the KMF. The metasomatism observed at the contact between the Hotazel and Mapedi formations is characterized predominantly by enrichment in Na, similar to what is observed in other parts of the KMF. Based on the study of the drill cores obtained from the contact between the Transvaal and Olifantshoek Supergroups in the Hotazel region, including geochemical and mineral analysis, results qualitatively characterize the presence of an alkali-rich assemblage around the contact between the two supergroups. This assemblage formed as a result of secondary enrichment in mainly Na, Ba, K, P, Al, Sr, amongst others. This is evident based on geochemical comparisons with samples of the same formation obtained from other parts of the KMF where similar alteration has occurred, or in some cases where rocks are pristine and lend themselves useful as protoliths for comparative studies. The minerals that formed as a result of the introduction of alkalis at the Hotazel-Mapedi contact include minerals like sugilite, aegirine, baryte, apatite, banalsite, albite, pectolite, and andradite. The occurrence of these secondary minerals geochemically parallels other alkali-rich metasomatic mineral assemblages observed in the broader KMF region and this could possibly imply that the KMF has been impacted by wide-scale alkali metasomatism by basinal brines produced as a result of thrusting and burial associated with the Kheis orogeny. The occurrence of these minerals adjacent to the Transvaal-Olifantshoek unconformity likely implies that the unconformity acted as a major conduit for fluid flow. It is likely that the extensive oxidation observed across the Transvaal-Olifantshoek contact occurred as a result of a prior hydrothermal event which involved oxidation and leaching of silica. This is because in order to form aegirine in such high concentrations, the Mapedi quartzites would have needed to be quite iron rich in order to serve as a suitable precursor to what is observed in the samples analyzed in this study.

More studies can be carried out to establish an even stronger link between the metasomatic assemblages observed in the different regions of the KMF. Such studies could include the dating of minerals such as sugilite in order to establish an age. The outcome of such studies may be able to establish if sugilite samples from across the KMF are of similar or substantially varying ages and this could shed even further light on the possibility of the KMF having been impacted by a large-scale alkali metasomatic event.

List of references

Beukes, N.J. (1983). *Paleoenvironmental setting of iron formations in the depositional basin of the Transvaal Supergroup, South Africa*. Developments in Precambrian Geology, v. 6, p. 131–209.

(Beukes, 1987)

Beukes, N.J., Dreyer, C.J.B. (1986). *Crocidolite deposits of the Pomfret Area, Griqualand West*. Mineral Deposits of Southern Africa, v. I, p. 911–21.

Beukes, N.J., Gutzmer, J., Mukhopadhyay, J. (2003). *The geology and genesis of high-grade hematite iron ore deposits.* Appl. Earth Sci. (Trans. Inst. Min. Metall. B)*,* v. 112, p. 18–25.

Beukes, N.J., Smit, C.A. (1987)*. New evidence for thrust faulting in Griqualand West, South Africa; implications for stratigraphy and the age of red beds.* South African Journal of Geology, v. 90, p. 378–394

Beukes, N.J., Swindell, E.P.W., Wabo, H. (2016). *Manganese Deposits of Africa*. Episodes, v. 39(2), p. 285–317.

Cairncross, B. (2017). *Connoisseur's Choice: Sugilite, Wessels Mine, Kalahari Manganese Field, Northern Cape Province*. South Africa. Rocks & Minerals, v. 92, p. 550-555.

Cornell, D.H., Schütte, S.S., & Eglinton, B.L. (1996). *The Ongeluk basaltic andesite formation on Griqualand West, South Africa: submarine alteration in a 2222 Ma Proterozoic sea*. Precambrian Research, v. 79, p. 101-123.

Cornell, D.H., Armstrong, R.A., Walraven, F. (1998)*. Geochronology of the Proterozoic Hartley Basalt Formation, South Africa: Constraints on the Kheis tectogenesis and the Kaapvaal Craton's earliest Wilson Cycle*. Journal of African Earth Sciences, v. 26, p. 5–27.

Costin, G., Fairey, B., Tsikos, H., Gucsik, A. (2016). *Tokyoite, As-Rich Tokyoite, and Noélbensonite: New occurrences from the Postmasburg Manganese Field, Northern Cape Province, South Africa*. The Canadian Mineralogist, v. 53, p. 981–990.

Cousins, D. (2016) *A stratigraphic, petrographic and geochemical study of the Gamagara Formation at the Maremane dome, Northern Cape province, South Africa*. Unpublished M.Sc. thesis, Rhodes University, South Africa. 124 pp.

De Villiers, J.E. (1943). *Gamagarite, a new vanadium mineral from the Postmasburg manganese deposits*. American Mineralogist, v. 28, p. 329–335.

Dixon, R. (1985). *Sugilite and associated minerals from Wessels mine, Kalahari manganese field*. Trans. Geol. Soc. S. Afr., v, 88, p. 11–18.

Dixon, R. (1989). *Sugilite and associated metamorphic silicate minerals from Wessels mine, Kalahari manganese field*. Bull. Geol. Surv. S. Afr., v. 93, 47 p.

Dunn, P. J. Peacor, D. R., Nelen, J. A., and Norberg, J. A. (1981) *Crystal-chemical data for schallerite, caryopilite and friedelite from Franklin and Sterling Hill, New Jersey*. Am. Min., v. 66, 1054–62.

Dunn, P.J., Brummer, J.J., Belsky, H. (1980). *Sugilite, a second occurrence: Wessels Mine, Kalahari Manganese Field, Republic of South Africa*. Can. Mineral., v. 18, p. 37–39.

Eriksson, P.G., Mazumder, R., Catuneanu, O., Bumby, A.J. and Ilondo, B.O. (2006) *Precambrian continental freeboard and geological evolution: A time perspective*. Earth- Sci. Rev. v. 79, 165-204.

Evans, D.A.D., Beukes, N.J., and Kirschvink, J.L. (2002). *Paleomagnetism of a lateritic paleoweathering horizon and overlying Paleoproterozoic red beds from South Africa: Implications for the Kaapvaal apparent polar wander path and a confirmation of atmospheric oxygen enrichment*. Journal of Geophysical Research, v. 107(B12), p. 2326.

Fairey, B. J., Timmerman, M. J., Sudo, M., & Tsikos, H. (2019). *The role of hydrothermal activity in the formation of karst-hosted manganese deposits of the Postmasburg Mn field, Northern Cape Province, South Africa*. Minerals, v. 9(7), p. 408.

Grant, J.A. (1986) *The isocon diagram; a simple solution to Gresens' equation for metasomatic alteration*. Econ. Geol., v. 81, p. 1976-1982.

Grant, J.A. (2005). *Isocon analysis: a brief review of the method and applications*. Physics and Chemistry of the Earth, v. 30, p. 997-1004

Grobbelaar, W.S., Burger, M.A., Pretorius, A.I., Marais, W., van Niekerk, I.J.M. (1995). *Stratigraphic and structural setting of the Griqualand West ant the Olifantshoek Sequences at Black Rock, Beeshoek and Rooinekke mines, Griqualand West, South Africa*. Mineral Deposita v. 30, p. 152-161.

Gumsley, A.P., Chamberlain, K.R., Bleeker, W., Söderlund, U., de Kock, M.O., Larsson, E.R. and Bekker, A. (2017). *Timing and tempo of the Great Oxidation Event*. Proceedings of the National Academy of Sciences, v. 114(8), p. 1811-1816.

Gutzmer, J., Beukes, NJ. (1995). *Fault-controlled metasomatic alteration of early Proterozoic sedimentary manganese ores in the Kalahari manganese field, South Africa*. Economic Geology, v. 90, p. 823–44.

Gutzmer, J., Beukes, NJ. (1996). *Mineral paragenesis of the Kalahari manganese field, South Africa*. Ore Geology Reviews, v. 11, p. 405–428.

Gutzmer, J., Beukes, NJ. (1997). *Effects of mass transfer, compaction and secondary porosity on hydrothermal upgrading of Paleoproterozoic sedimentary manganese ore in the Kalahari manganese field, South Africa*. Mineralium Deposita, v. 32, p. 250–256.

Land, J. S., Tsikos, H., Cousins, D., Luvizotto, G., & Zack, T. (2017). *Origin of red beds and paleosols in the Palaeoproterozoic Transvaal and Olifansthoek Supergroups of South Africa: provenance versus metasomatic controls*. Geological Journal, v. *53*(1), p. 191–202.

Mhlanga, X.R. (2021). *A reappraisal of the origin of the Hotazel Fe-Mn Formation in an evolving early Earth system through the application of mineral-specific geochemistry, speciation techniques and stable isotope systematics*. PhD thesis (unpublished) Rhodes University.

Miyano, T., & Beukes, N.J. (1984). *Phase relations of stilpnomelane, ferriannite and riebeckite in very low-grade metamorphosed ironformations*. Transaction of Geological Society of South Africa, v. 87, p. 111- 124.

Monku, M. (2016). *The distribution and origin of Barium- rich occurrences in the rocks of the basal lithological unit of the Olifantshoek Supergroup, Northern Cape*. Honors thesis (unpublished) Rhodes University.

Moore, J.M., Kuhn, B.K., Mark, D.F., & Tsikos, H. (2011). *A sugilite-bearing assemblage from the Wolhaarkop breccia, Bruce iron-ore mine, South Africa: Evidence for alkali metasomatism and 40Ar–39Ar dating*. European Journal of Mineralogy v. 23, p. 661–673.

Moore, J.M., Tsikos, H., Polteau, S. (2001). *Deconstructing the Transvaal Supergroup, South Africa: implications for Palaeoproterozoic palaeoclimate models*. Journal of African Earth Sciences, v. 33, p. 437–444.

Polteau, S., Moore, J.M., Tsikos, H. (2006). *The geology and geochemistry of the Palaeoproterozoic Makganyene diamictite*. Precambrian Res. v. 148, p. 257–274.

Pourmand, A., Dauphas, N., Ireland, T.J. (2012). *A novel extraction chromatography and MC-ICP-MS technique for rapid analysis of REE, Sc and Y: Revising CI-chondrite and Post-Archean Australian Shale (PAAS) abundances*. Chemical Geology, v. 291, p.38-54.

Smith, A.J.B., & Beukes, N.J. (2016) *Palaeoproterozoic banded iron formation-hosted high-grade hematite iron ore deposits of the Transvaal Supergroup, South Africa*. Episodes. V. 39, p. 269-284.

Stowe, C. W. (1986). *Synthesis and interpretation of structures along the north-eastern boundary of the Namaqua Tectonic Province, South Africa*. Trans. geol. Soc. S. Afr. v. 89, p. 185-198.

Tsikos, H., Beukes, NJ., Moore, JM., Harris, C. (2003). *Deposition, diagenesis, and secondary enrichment of metals in the Paleoproterozoic Hotazel iron Formation, Kalahari Manganese Field, South Africa*. Economic Geology, v. 98, p. 1449–62.

Tsikos, H., & Moore, J.M. (1997). *Petrography and geochemistry of the Paleoproterozoic Hotazel iron formation, Kalahari Manganese Field, South Africa*: *Implications for Precambrian manganese metallogenesis*. Economic geology, v. 92, p. 87–97.

Tsikos, H. & Moore, JM. (2005). *Sodic metasomatism in the Palaeoproterozoic Hotazel iron Formation, Transvaal Supergroup, South Africa: implications for fluid-rock interaction in the Kalahari manganese field*. Geofluids, v. 5, p. 264–271.

Cape Minerals. (2017). *The Kalahari Manganese Fields*. Retrieved from: https://www.capeminerals.co.za/the-kalahari-manganese-fields . Accessed on: 03/03/2022.

Van Wyk, J.P. (1980). *The geology of the area Rooinekke-Matsap-Wolhaarkop in Northern Cape with special reference to the Koegas Subgroup, Transvaal Supergroup*. M.Sc. thesis (unpublished) R.A.U., Johannesburg.

Yamaguchi, K. E., & Ohmoto, H. (2006). *Geochemical and isotopic constraints on the origin of Paleoproterozoic red shales of the Gamagara/Mapedi Formation, Postmasburg Group, South Africa*. South African Journal of Geology, v. *109*(1–2), p. 123–138.

Appendix A

Table 3. Major element oxide abundances of samples from this study.

Rock type	Sample	ID	Al_2O_3 (%)	CaO (%)	Cr2O3 (%)	Fe_2O_3 (%)	K_2O (%)	MgO (%)	MnO (%)	Na_2O (%)	P_2O_5 (%)	SiO_2 (%)	TiO_2 (%)	L.O.I. (%)	Sum Of Conc. (%)
massive hematite	1	DB87A	1.34	1.26	bdl	66.98	0.01	0.23	22.98	0.19	0.04	5.27	0.04	0.77	99.11
quartzite	2	DB87D	3.69	1.01	bdl	40.64	0.06	0.39	0.11	10.13	0.31	42.56	0.07	1.25	100.21
quartzite	3	DB87L	1.43	0.24	bdl	30.98	0.75	bdl	0.03	11.50	0.01	55.23	0.11	0.11	100.38
shale	4	DB87N1	17.68	0.33	0.01	21.05	1.78	1.09	0.06	6.51	0.04	50.22	0.76	1.30	100.82
shale	5	DB87N2	17.81	0.65	bdl	1.54	0.42	1.82	0.06	11.27	0.23	65.46	0.74	0.90	100.89
quartzite	6	UB189E	3.33	0.45	bdl	8.37	2.64	0.26	0.05	3.33	bdl	81.75	0.13	-0.03	100.28
quartzite	7	UB189B	5.93	0.99	0.01	4.56	3.64	0.48	0.08	5.61	bdl	77.26	0.19	0.40	99.13
shale	8	UB189M1	15.03	0.62	0.02	3.41	4.29	2.25	0.03	0.06	0.36	68.41	1.79	2.99	99.25
shale	9	UB189M2	14.35	0.31	0.02	16.22	4.37	0.57	0.02	0.03	0.21	60.18	1.68	2.53	100.48
massive hematite	10	UB189A	0.89	5.55	bdl	49.75	0.06	0.21	33.93	0.12	0.08	8.00	0.12	0.40	99.10
quartzite	11	W351C1	0.16	0.46	bdl	16.87	1.89	bdl	0.21	6.21	bdl	73.01	0.05	0.32	99.18
quartzite	12	W361C2	0.05	0.28	bdl	3.04	0.13	0.14	0.25	0.87	bdl	95.89	0.06	-0.17	100.54
quartzite	13	W351E	0.17	2.26	bdl	22.94	0.04	0.27	0.25	5.66	0.02	68.64	0.13	0.08	100.46
shale	14	W351L	6.81	0.15	bdl	8.03	1.68	0.26	0.04	0.11	0.09	81.64	0.30	0.99	100.10
massive hematite	15	W351A	0.28	0.68	bdl	94.55	0.01	0.02	3.00	0.03	0.06	1.12	0.04	0.26	100.04
quartzite	16	DB88C	0.24	1.59	bdl	16.92	0.13	0.02	0.04	6.17	0.04	74.38	0.03	0.40	99.96
quartzite	17	DB88B1	4.83	10.33	bdl	4.69	3.05	bdl	0.12	7.04	0.90	62.90	0.04	0.44	94.33
massive hematite	18	DB88A	0.89	0.73	bdl	84.66	0.02	0.02	0.65	0.13	0.12	1.24	0.04	0.50	89.00
massive hematite	19	DB88B2	2.68	9.47	bdl	72.23	0.02	0.18	0.42	0.11	3.92	4.33	0.10	1.19	94.63
quartzite	20	DB88H	0.44	1.86	bdl	34.10	0.27	0.89	0.19	10.69	bdl	52.11	0.04	0.20	100.78
shale	21	DB88K	18.51	0.33	0.01	21.42	2.61	0.20	0.02	6.17	0.08	49.03	0.85	1.54	100.78
quartzite	22	DB89J	0.37	3.52	0.01	12.37	0.28	bdl	0.02	5.64	bdl	78.83	0.10	0.22	101.37
quartzite	23	DB89E	0.15	0.48	bdl	44.98	0.01	0.06	2.46	10.03	0.17	42.55	0.01	-0.02	100.88
shale	24	DB89L	14.89	0.16	0.01	17.47	2.09	0.32	0.01	4.64	0.11	59.99	0.73	1.23	101.66
massive hematite	25	DB89C	0.45	2.75	bdl	48.04	-0.01	0.05	43.97	bdl	0.03	4.27	0.10	0.29	99.94

- All data reported as weight percent (Wt.%). Total Fe reported as Fe_2O_3.

Table 4. Trace element abundances of samples from this study.

Rock type	Sample	ID	Sc (ppm)	V (ppm)	Cr (ppm)	Co (ppm)	Ni (ppm)	Cu (ppm)	Zn (ppm)	Rb (ppm)	Sr (ppm)	Y (ppm)	Zr (ppm)	Nb (ppm)	Mo (ppm)	Cs (ppm)	Ba (ppm)
massive hematite	1	DB87A	3.01	23.44	18.82	93.52	34.90	79.03	49.48	0.52	2452.71	18.93	99.41	0.78	2.94	0.07	22785.08
quartzite	2	DB87D	3.04	20.59	33.62	4.15	7.49	49.75	154.19	1.06	83.91	3.02	91.00	1.27	3.03	0.05	251.63
quartzite	3	DB87L	4.05	28.84	38.81	2.10	8.23	36.69	69.74	3.41	84.39	1.04	60.40	1.49	1.59	0.12	55.70
shale	4	DB87N1	16.61	85.55	125.28	5.45	19.23	188.69	36.68	79.08	124.04	9.31	157.21	13.74	1.54	7.67	247.96
shale	5	DB87N2	14.18	31.13	86.92	1.94	17.32	14.64	64.22	3.82	169.98	4.65	141.96	5.78	2.20	2.05	339.51
quartzite	6	UB189E	6.92	30.05	68.45	7.57	18.78	380.10	18.92	31.37	192.48	5.22	37.20	2.09	1.86	0.16	140.67
quartzite	7	UB189B	6.78	24.15	74.17	11.03	25.72	71.22	38.32	20.51	107.16	10.81	58.17	4.36	2.18	1.29	115.26
shale	8	UB189M1	25.11	201.11	218.83	22.56	31.15	56.55	91.28	131.43	180.48	27.19	341.80	53.88	1.45	6.55	5388.01
shale	9	UB189M2	23.30	202.34	179.70	9.93	21.74	35.56	21.48	137.64	36.14	25.41	334.09	52.37	1.33	7.56	553.48
massive hematite	10	UB189A	9.66	32.54	36.35	169.50	36.80	552.63	55.52	1.67	717.05	16.59	65.09	2.46	4.29	0.39	18069.02
quartzite	11	W351C1	3.56	18.44	58.88	2.60	9.48	45.48	24.65	12.73	263.02	1.65	105.88	0.88	2.01	0.22	57.01
quartzite	12	W361C2	4.85	22.77	76.65	3.17	10.49	39.51	15.50	0.80	19.42	1.27	104.04	1.34	2.83	-	26.59
quartzite	13	W351E	3.62	27.93	97.36	3.38	10.66	25.20	16.14	1.45	39.63	1.42	133.93	1.59	2.06	0.05	187.36
shale	14	W351L	9.79	101.69	83.14	6.31	19.82	50.88	14.66	63.45	22.26	6.57	88.75	5.80	3.11	1.77	148.38
massive hematite	15	W351A	1.71	33.58	24.75	26.14	11.66	43.13	15.17	0.46	205.38	1.31	30.35	1.28	3.88	0.18	3238.90
quartzite	16	DB88C	3.52	18.91	37.33	3.78	10.99	114.30	85.36	3.62	1402.78	0.99	39.41	0.62	2.44	0.19	2214.93
quartzite	17	DB88B1	3.11	15.23	11.30	2.41	8.67	26.56	82.02	17.35	9913.57	1.31	55.53	0.38	1.41	0.42	11468.74
massive hematite	18	DB88A	1.34	32.35	27.01	18.50	12.63	57.48	24.42	0.71	2117.95	1.99	19.96	0.84	3.05	0.12	39400.42
massive hematite	19	DB88B2	1.53	90.08	61.14	15.29	13.15	46.50	23.64	0.74	6081.17	6.74	46.45	1.98	4.45	0.12	20796.05
quartzite	20	DB88H	3.62	52.78	36.87	12.26	22.43	118.57	36.64	3.74	371.20	0.66	46.68	0.76	1.67	0.14	2213.67
shale	21	DB88K	17.52	137.14	143.62	4.87	19.52	63.02	12.04	102.08	86.72	11.03	171.38	14.72	1.67	3.81	461.58
quartzite	22	DB89J	3.67	33.57	85.82	2.51	7.42	28.17	21.21	2.04	91.58	1.64	128.65	1.72	1.72	-	18.69
quartzite	23	DB89E	8.18	17.19	196.87	3.36	11.29	56.48	13.98	30.88	242.12	9.67	250.76	2.89	1.47	0.24	23.81
shale	24	DB89L	15.65	141.68	145.48	19.96	24.75	39.16	13.38	88.56	49.36	13.55	207.08	12.78	1.43	3.72	230.25
massive hematite	25	DB89C	21.83	24.81	24.16	173.99	23.77	298.16	66.96	0.24	312.95	70.46	136.78	1.88	4.25	0.04	2526.53

- All data reported as parts per million (ppm).

Table 5. Rare earth element abundances of samples from this study.

ID	La (ppm)	Ce (ppm)	Pr (ppm)	Nd (ppm)	Sm (ppm)	Eu (ppm)	Gd (ppm)	Tb (ppm)	Dy (ppm)	Ho (ppm)	Er (ppm)	Tm (ppm)	Yb (ppm)	Lu (ppm)	Hf (ppm)	Ta (ppm)	Pb (ppm)	Th (ppm)	U (ppm)
DB87A	20.71	34.48	4.85	20.01	4.43	1.28	4.57	0.65	4.14	0.84	2.44	0.37	2.58	0.37	2.21	0.07	845.65	0.73	0.59
DB87D	4.24	6.13	0.83	2.79	0.54	0.07	0.49	0.09	0.49	0.11	0.31	0.04	0.26	0.05	2.79	0.12	55.59	1.83	0.61
DB87L	1.83	4.91	0.25	0.85	0.14	0.05	0.12	0.02	0.18	0.04	0.13	0.03	0.20	0.03	1.45	0.11	11.07	2.33	0.10
DB87N1	34.94	69.28	6.43	21.84	2.85	0.62	2.36	0.28	1.59	0.38	1.15	0.16	1.42	0.22	4.37	0.98	39.90	15.65	1.07
DB87N2	14.43	35.04	3.71	24.66	1.99	0.78	1.37	0.45	1.33	0.38	0.56	0.13	0.55	0.17	1.98	0.85	1.39	7.49	0.13
UB189E	4.06	7.52	0.84	2.39	0.23	0.07	0.34	0.07	0.68	0.16	0.65	0.09	0.76	0.10	1.14	0.14	8.79	2.85	0.12
UB189B	1.91	3.70	1.35	4.93	0.95	0.21	0.86	0.16	1.46	0.32	1.20	0.16	1.14	0.20	1.66	0.31	3.28	3.90	0.04
UB189M1	66.31	186.50	14.54	48.58	8.34	1.68	6.54	0.76	4.41	1.00	2.60	0.40	2.72	0.42	8.63	2.95	6.29	13.50	3.65
UB189M2	50.89	132.77	11.39	38.93	6.71	1.68	5.03	0.75	4.25	0.87	2.62	0.33	2.64	0.37	8.49	2.77	12.44	12.75	1.49
UB189A	11.40	39.31	2.84	11.50	2.27	0.76	2.38	0.37	2.13	0.42	1.34	0.21	1.13	0.20	1.40	0.14	43.39	1.87	0.26
W351C1	2.87	3.19	0.37	1.32	0.27	0.05	0.21	0.03	0.25	0.05	0.18	0.04	0.25	0.04	2.49	0.10	2.69	1.35	0.04
W361C2	1.21	2.74	0.22	0.74	0.12	0.06	0.13	0.04	0.17	0.07	0.14	0.02	0.25	0.04	2.64	0.10	1.91	1.11	0.09
W351E	2.14	3.17	0.29	1.03	0.25	0.02	0.22	0.03	0.22	0.07	0.18	0.04	0.25	0.04	3.23	0.16	5.47	1.65	0.23
W351L	17.08	40.47	4.40	18.26	4.22	0.85	2.72	0.32	1.54	0.29	0.75	0.13	0.90	0.15	2.42	0.39	6.66	6.95	0.69
W351A	9.66	4.24	1.44	4.42	0.60	0.13	0.40	0.05	0.30	0.06	0.19	0.02	0.17	0.03	0.31	0.10	99.60	0.67	0.18
DB88C	2.40	2.35	0.25	0.88	0.30	0.08	0.22	0.03	0.22	0.04	0.14	0.03	0.19	0.03	1.03	0.03	23.33	0.82	0.04
DB88B1	5.39	3.93	0.75	2.16	0.51	0.20	0.18	0.05	0.27	0.06	0.20	-	0.14	0.02	1.76	0.08	309.68	0.66	0.13
DB88A	7.81	23.83	1.91	6.54	0.97	0.54	0.72	0.09	0.53	0.09	0.26	0.04	0.27	0.03	0.22	0.06	182.73	0.62	0.19
DB88B2	11.02	13.01	2.42	8.46	1.46	0.44	1.45	0.21	1.19	0.23	0.66	0.10	0.56	0.08	0.90	0.28	150.73	4.52	0.37
DB88H	3.06	2.66	0.38	0.92	0.13	0.06	0.11	0.03	0.12	0.03	0.06	0.02	0.12	0.01	1.07	0.06	44.29	1.23	0.28
DB88K	39.75	76.08	7.24	23.39	3.51	0.76	2.59	0.31	2.07	0.46	1.36	0.23	1.59	0.26	4.49	1.16	47.85	17.86	1.61
DB89J	3.61	8.12	0.48	1.53	0.34	0.02	0.27	0.06	0.27	0.09	0.23	0.03	0.30	0.05	3.21	0.15	3.40	1.77	0.87
DB89E	7.04	11.62	1.86	7.56	1.46	0.32	1.40	0.25	1.71	0.38	1.20	0.17	1.36	0.19	6.32	0.51	3.05	8.37	0.30
DB89L	36.74	75.64	7.07	23.86	3.97	0.82	3.15	0.46	2.81	0.61	1.64	0.26	1.89	0.32	5.65	0.92	9.77	15.28	1.43
DB89C	20.43	56.88	8.16	35.64	10.09	2.83	10.33	1.93	13.21	2.51	7.58	1.09	7.53	1.19	1.77	0.10	154.37	0.67	0.43

- All data reported as parts per million (ppm).

Table 6. Major oxide abundances (in wt.%) for Gloria Mine BIF and lutite (Mhlanga, 2021) .

	Fe_2O_3	MnO2	TiO_2	CaO	K_2O	P_2O_5	SiO_2	Al_2O_3	MgO	Na_2O	LOI
Hotazel BIF averages	45.49	0.64	0.01	7.83	0.04	0.10	35.46	0.23	1.56	0.03	7.76
Hotazel Hematite lutite averages	34.53	14.91	0.01	11.46	0.14	0.06	15.52	0.25	4.55	0.65	17.18
Hotazel Mn ore averages	16.24	36.19	0.01	15.46	0.10	0.04	8.52	0.22	3.99	0.04	19.45

Table 7. Trace element abundances (in ppm) for Gloria Mine BIF and lutite (Mhlanga, 2021).

	V	Cr	Co	Ni	Cu	Zn	Y	Zr	Mo	Pb	Sr	Ba
Hotazel BIF averages	9.97	23.71	3.79	12.84	7.30	26.83	8.80	5.18	1.79	4.04	168.30	63.51
Hotazel Hematite lutite averages	9.18	18.18	50.29	13.40	8.19	32.30	8.01	5.28	1.85	2.59	203.87	383.18
Hotazel Mn ore averages	8.57	24.31	40.78	19.81	7.53	45.77	5.75	4.25	2.86	3.74	259.08	245.19

Table 8. Major oxide abundances (in wt.%) for Postmasburg quartzites (Monku, 2016).

	n=1	n=2	n=3	n=4	n=5	n=6	n=7	n=8	n=9	n=10	n=11	n=12	n=13	n=14	n=15	average
Al_2O_3	6.09	0.36	0.53	0.27	0.56	0.31	0.31	0.80	0.33	0.40	0.23	0.24	1.86	0.34	4.05	1.11
CaO	0.14	0.04	0.03	0.03	0.03	0.03	0.02	0.04	0.03	0.07	0.03	0.02	0.03	0.03	0.04	0.04
Fe_2O_3	15.15	1.21	1.22	3.79	3.58	5.92	1.15	0.89	2.21	13.31	12.39	3.96	8.38	2.64	21.97	6.52
K_2O	0.05	0.10	0.14	0.08	0.15	0.08	0.07	0.22	0.09	0.10	0.05	0.06	0.52	0.09	0.07	0.12
MgO	3.51	0.05	0.06	0.04	0.05	0.05	0.05	0.05	0.04	0.04	0.04	0.04	0.05	0.04	0.05	0.28
MnO	0.05	0.02	0.02	0.04	0.04	0.04	0.00	0.01	0.04	0.05	0.04	0.04	0.04	0.04	0.03	0.03
Na_2O	0.00	0.00	0.00	0.00	0.00	0.00	0.09	0.00	0.00	0.00	0.00	0.00	0.00	0.00	0.00	0.01
P_2O_5	0.05	0.01	0.01	0.01	0.01	0.01	0.01	0.01	0.01	0.05	0.01	0.01	0.01	0.01	0.07	0.02
SiO_2	73.26	92.05	91.61	95.04	95.03	90.81	66.41	97.26	91.60	86.04	87.24	95.11	88.80	96.54	72.58	87.96
TiO_2	0.33	0.03	0.08	0.04	0.07	0.03	0.08	0.08	0.04	0.04	0.03	0.01	0.04	0.03	0.93	0.12

- bdl = below detection limits

Table 9. Trace element abundances (in ppm) for Postmasburg quartzites (Monku, 2016).

	n=1	n=2	n=3	n=4	n=5	n=6	n=7	n=8	n=9	n=10	n=11	n=12	n=13	n=14	n=15	average
Sc	13.39	3.77	3.34	3.18	3.38	2.78	2.14	3.46	2.25	3.14	2.71	2.96	3.65	2.57	10.16	4.19
V	110.68	15.72	18.09	21.70	18.72	24.79	14.85	11.04	17.90	35.50	66.57	21.27	33.43	20.42	202.61	42.22
Cr	1157.67	47.25	466.38	74.22	76.16	70.49	48.85	52.39	61.61	78.07	83.17	58.04	91.58	80.39	236.62	178.86
Co	70.28	1.83	1.88	2.62	13.42	2.48	1.94	1.32	2.23	2.60	1.98	2.12	2.18	3.03	2.40	7.49
Ni	426.52	18.67	13.37	16.92	19.37	16.47	14.66	14.47	19.97	20.44	15.62	18.05	15.02	20.73	13.84	44.27
Cu	71.60	82.93	51.33	72.40	30.41	86.61	105.92	17.92	40.58	35.74	25.84	94.12	80.90	25.47	24.74	56.43
Zn	66.13	43.55	28.06	52.66	51.53	24.20	118.42	20.53	56.31	40.05	59.15	57.82	54.78	31.87	44.31	49.96
Pb	0.95	1.36	1.42	1.53	2.17	1.22	1.36	1.21	0.84	1.75	1.33	1.15	1.49	1.38	3.30	1.50
Ba	21.18	28249.70	28609.80	4300.90	759.70	10918.30	146274.40	2125.20	24197.80	91.56	65.83	2697.10	320.48	42.70	96.36	16584.73
Rb	2.48	3.73	4.63	2.27	3.69	2.29	2.47	6.13	2.32	3.04	1.53	1.93	15.40	2.50	1.72	3.74
Sr	2.87	384.26	390.87	57.87	14.02	119.85	2768.58	23.05	313.57	5.04	5.83	34.24	9.06	12.73	333.72	298.37
Y	11.51	2.79	2.54	2.13	2.10	1.18	1.73	1.49	1.06	1.60	1.41	1.10	1.23	1.29	7.53	2.71
Zr	63.77	62.62	52.67	74.10	79.66	35.49	35.34	49.04	35.43	59.15	41.02	28.81	40.73	41.66	167.44	57.80
Hf	1.73	1.23	1.45	1.76	1.97	0.88	0.84	1.41	1.00	1.64	1.06	0.72	1.12	1.13	3.93	1.46
Ta	0.20	0.06	0.07	0.05	0.09	0.05	0.05	0.14	0.08	0.07	0.06	0.04	0.06	0.05	1.34	0.16
Nb	3.41	11.17	2.46	2.27	4.42	3.36	3.58	2.83	3.38	5.72	5.19	3.29	7.13	2.21	25.85	5.75
Th	2.48	1.08	1.50	1.00	1.10	1.43	0.82	1.43	1.20	1.31	1.48	0.84	1.24	1.37	4.90	1.55
U	0.67	0.22	0.47	0.22	0.70	0.34	0.16	0.21	0.20	0.42	0.25	0.16	0.28	0.21	0.58	0.34

Table 10. Bulk geochemical values (in wt.%) for hematite samples and Gloria Mine lutite protolith.

	"Ore"	*"Waste"*	Slope
SiO_2	4.04	15.52	3.84
Al_2O_3	1.09	0.25	0.23
TiO2	0.07	0.01	0.14
Fe_2O_3	69.37	34.53	0.50
MnO	17.49	14.91	0.85
MgO	0.12	4.55	38.76
CaO	3.41	11.46	3.36
K_2O	0.02	0.14	7.84
Na_2O	0.12	0.65	5.68
P_2O_5	0.71	0.06	0.09
LOI	0.57	17.18	30.25
V	0.003947	0.000917947	0.23
Sr	0.19812	0.020386711	0.10
Pb	0.009805	0.000258761	0.03
Co	0.008282	0.005028737	0.61
Cu	0.017949	0.000818711	0.05
Ba	1.780267	0.038317789	0.02
Zn	0.00392	0.003229526	0.82

Table 11. Scaling factors for hematite samples and Gloria Mine lutite protolith.

Factor	Element/Oxide	Scaled Ore	Scaled waste	Slope
1	SiO_2	4.0	15.5	3.8
1	Al_2O_3	1.1	0.3	0.2
100	TiO_2	7.3	1.0	0.1
1	Fe_2O_3	34.7	17.3	0.5
1	MnO	17.5	14.9	0.9
1	MgO	0.1	4.6	38.8
1	CaO	3.4	11.5	3.4
100	K_2O	1.8	14.3	7.8
10	Na_2O	1.2	6.5	5.7
20	P_2O_5	14.2	1.2	0.1
1	LOI	0.6	17.2	30.3
250	V	1.0	0.2	0.2
50	Sr	9.9	1.0	0.1
200	Pb	2.0	0.1	0.0
200	Co	1.7	1.0	0.6
200	Cu	3.6	0.2	0.0
10	Ba	17.8	0.4	0.0
200	Zn	0.8	0.6	0.8

Table 12. Trace element abundances (in wt.%) for drill cores DB89 and W351 provided by Hotazel Mine.

	As	BaO	Co	Cr	Cu	Ni	Pb	SrO	V_2O_5	Zn
DB89	0.0128	<0.0058	0.0167	<0.0126	<0.0027	<0.0096	<0.0322	<0.0058	<0.0346	<0.0151
W351	0.0129	<0.0058	0.0168	<0.0126	<0.0027	<0.0096	<0.0322	<0.0058	<0.0346	<0.0151